

AD-A120 227

NDT TECHNOLOGIES INC SOUTH WINDSOR CT
ELECTROMAGNETIC INSPECTION OF WIRE ROPES USING SENSOR ARRAYS.(U)
JUL 82 H R WEISCHEDEL

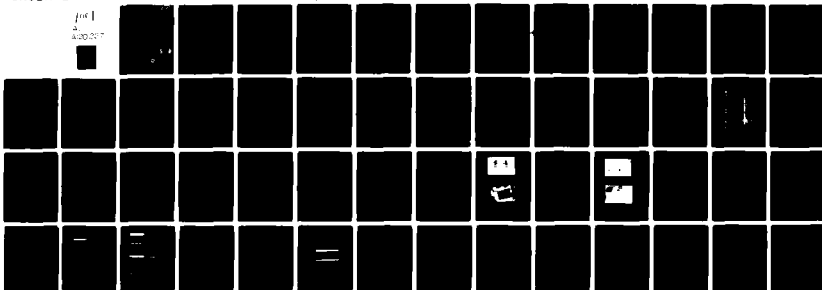
F/G 14/2

N00014-82-C-0146

NL

UNCLASSIFIED

for 1
Robert



END
DATE
FILMED
11-82
DTIC



Contract N00014-82-C-0146

AD A120227

ELECTROMAGNETIC INSPECTION OF WIRE ROPES USING SENSOR ARRAYS

Herbert R. Weischedel
NDT Technologies, Inc.
125 Mohegan Trail
South Windsor, CT 06074

31 July 1982

Final Report for Period 1 January 1982 - 31 July 1982

Prepared for

OFFICE OF NAVAL RESEARCH
DEPARTMENT OF THE NAVY
800 N. Quincy Street
Arlington, Virginia 22217

DTIC
ELECTE
S D
OCT 14 1982
D

DTIC FILE COPY

 NDT technologies, inc.
125 mohegan trail
south windsor, ct. 06074
(203) 644-8507

DISTRIBUTION STATEMENT A
Approved for public release;
Distribution Unlimited

82 10 13 031

REPORT DOCUMENTATION PAGE		READ INSTRUCTIONS BEFORE COMPLETING FORM		
1. REPORT NUMBER N00014-82-C-0146	2. GOVT ACCESSION NO. AD-A120 227	3. RECIPIENT'S CATALOG NUMBER		
4. TITLE (and Subtitle) ELECTROMAGNETIC INSPECTION OF WIRE ROPES USING SENSOR ARRAYS		5. TYPE OF REPORT & PERIOD COVERED Final 1 Jan 82 to 31 Jul 82		
7. AUTHOR(s) Herbert R. Weischedel		6. PERFORMING ORG. REPORT NUMBER		
9. PERFORMING ORGANIZATION NAME AND ADDRESS NDT Technologies, Inc. 125 Mohegan Trail South Windsor, CT 06074		8. CONTRACT OR GRANT NUMBER(s) N00014-82-C-0146		
11. CONTROLLING OFFICE NAME AND ADDRESS Office of Naval Research Department of the Navy 800 N Quincy St., Arlington, VA 22217		10. PROGRAM ELEMENT, PROJECT, TASK AREA & WORK UNIT NUMBERS		
14. MONITORING AGENCY NAME & ADDRESS (if different from Controlling Office)		12. REPORT DATE 31 July 1982		
		13. NUMBER OF PAGES 56		
		15. SECURITY CLASS. (of this report)		
		15a. DECLASSIFICATION/DOWNGRADING SCHEDULE		
16. DISTRIBUTION STATEMENT (of this Report)				
<table border="1"> <tr> <td> <p>DISTRIBUTION STATEMENT A</p> <p>Approved for public release; Distribution Unlimited</p> </td> </tr> </table>				<p>DISTRIBUTION STATEMENT A</p> <p>Approved for public release; Distribution Unlimited</p>
<p>DISTRIBUTION STATEMENT A</p> <p>Approved for public release; Distribution Unlimited</p>				
17. DISTRIBUTION STATEMENT (of the abstract entered in Block 20, if different from Report)				
18. SUPPLEMENTARY NOTES				
19. KEY WORDS (Continue on reverse side if necessary and identify by block number) Nondestructive Testing (NDT); electromagnetic NDT methods; defect characterization; wire rope				
20. ABSTRACT (Continue on reverse side if necessary and identify by block number) A rational and reliable method for the inspection of wire ropes is presently not available. Both, visual and electromagnetic inspection methods depend on the intuition of the inspector. The research in this report establishes feasibility of a new automatic defect characterization method for the electromagnetic inspection of wire ropes. The new method				

SECURITY CLASSIFICATION OF THIS PAGE(When Data Entered)

promises a considerable improvement of inspection reliability as compared to present procedures. The technique which has been validated consists of (1) sensing magnetic leakage fields caused by rope defects with an array of test coils, (2) extracting pertinent signal parameters from the test signals, and (3) deriving an estimate of flaw parameters by a transformation of the signal parameter vector. Laboratory instruments were designed and built to implement the proposed approach and to demonstrate its feasibility.

Accession For	
NTIS GRA&I	<input checked="" type="checkbox"/>
DTIC TAB	<input type="checkbox"/>
Unannounced	<input type="checkbox"/>
Justification	
By <i>Per ltr. on file</i>	
Distribution/	
Availability Codes	
Dist	Avail and/or Special
<i>A</i>	



SECURITY CLASSIFICATION OF THIS PAGE(When Data Entered)

Contents

		<u>Page</u>
Paragraph 1	INTRODUCTION	1
2	THE LEAKAGE FLUX (DC) METHOD FOR WIRE ROPE INSPECTION	4
3	AUTOMATIC DEFECT CHARACTERIZATION	5
4	THE PROPOSED AUTOMATIC DEFECT CHARACTERIZATION METHOD	7
4.1	Sensor Design	12
4.1.2	Design Criteria	14
4.2	Test Signal Conditioning	20
4.2.1	Test Signal Modification	23
4.2.2	Peak Sample/Hold Circuit	25
5	EXPERIMENTAL RESULTS	27
5.1	Hardware Implementation	27
5.2	Experimental Results from a Rope Model	32
5.3	Experimental Results from a Test Rope	37
5.4	Signal-to-Noise Ratio and Repeatability	40
6	SUMMARY AND CONCLUSION	43
Appendix A	COMPUTER SIMULATION PROGRAM	46

1. INTRODUCTION

Wire ropes are used in numerous military and industrial applications. Almost without exception, failure of wire rope poses an extremely serious safety hazard and periodic inspections are mandated by safety authorities. And yet, a reliable and rational method for inspecting wire ropes is presently not available. Both, visual and electromagnetic inspection methods depend to a great extent on the intuition of the inspector. Serious accidents, costly unscheduled equipment downtime and the presently usual premature replacement of wire ropes are all consequences of this situation.

A wide variety of nondestructive test methods for the inspection of wire ropes have been tried. However, because of the complicated and inhomogeneous structure of wire ropes, electromagnetic inspection at the present time is the only feasible method. A review of AC and DC electromagnetic procedures for wire rope testing is presented by Wait (1). Since AC testing cannot detect small flaws such as broken wires, DC testing has become the preferred method in more recent times. This investigation concerns DC instruments.

The so-called DC method of electromagnetic wire rope inspection belongs to the class of magnetic leakage flux methods (also called magnetic stray flux or magnetic perturbation methods). A comprehensive review of the state-of-the-art of these methods is given in (2).

For the inspection of non-homogeneous ferrous materials, such as cast or as-rolled materials, flux perturbation methods offer a

(1) J.R.Wait, "Review of Electromagnetic Methods in Nondestructive Testing of Wire Ropes," Proc. of the IEEE, Vol. 67, No.6, pp. 892-903, June 1979

(2) R.E.Beissner, G.A.Matzkanin and C.M.Teller, "NDE Applications of Magnetic Leakage Field Methods, A State-of-the-Art Survey," Southwest Research Institute, San Antonio, Texas, January 1980

superior signal-to-noise ratio (SNR). As compared to eddy current methods, SNR improvements by a factor of four to eight have been reported for flux perturbation methods (1), (3). Wire rope has a highly non-homogeneous structure, and the above observations are borne out by similar experiences in electromagnetic rope testing. The SNR and resolving power of the DC method (a flux perturbation method) are greatly superior to the AC method (an eddy current type method).

A dominant characteristic of data readout from most non-destructive tests is their heavy dependence on visual interpretation of graphically displayed data with considerable reliance on the human operator. Data interpretation is an art rather than a science and the experienced human operator is an essential component of the inspection process subject to all the subjectivity, fallability and variability of humans. The present state-of-the-art of gleaning useful information from tests is far from satisfactory.

The mere detection of a defect is often not sufficient. Usually, to properly assess its severity, one needs to know not only the type of defect present, but also its location and size. At present, the magnetic leakage field method, like all other NDE methods, fails to satisfy all of these requirements to the degree desired.

Four stages of defect characterization can be defined:

- The first is defect detection. Most NDE methods for wire rope inspection are restricted to this first stage. Defect detection

(3) Foerster, F., "Theoretical and Experimental Developments in Magnetic Stray Flux Techniques for Defect Detection", British J. NDT, November 1975, pp. 168-171.

relies almost exclusively on relative signal amplitudes, and an SNR greater than 1 is the dominant criterium for flaw detectability. Because of the sometimes unsatisfactory SNR in wire rope inspection, even this first stage of defect identification leaves something to be desired.

- The second step is defect identification, i.e. the determination of the type of defect present. In the case of wire rope, the following defect categories can usually be distinguished from the test signal waveshape: 1. Broken wires, including missing pieces of wires, broken strands and cores. 2. Corrosion and abrasion (however, tightly spaced broken wires might have a similar waveshape). Other defects, such as rope deformation, kinks, heat damage, etc. can usually be detected, however, the nature of the defect has to be ascertained by a visual examination. Particular problems arise when different types of flaws are superimposed, for instance rust and broken wires. Under these conditions a defect identification can become difficult. If it is possible, a visual inspection of suspicious areas is always desirable. Some progress has been made in this area (4), (5), and even a flaw catalog has been published (6).
- The third step is a quantitative defect characterization. Usually it is desired to determine the size and location of the defect.

(4)H. Babel, "Destructive and Nondestructive Test Methods for the Determination of the Life Expectancy of Wire Ropes, Part II", (in German), Draht, Vo. 30, No. 4, pp.354-359, 1979

(5)R. Kurz, "The Magnetic Induction Method for Cable Testing, Experience and Future Prospects", Fourth International Congress of Transportation by Rope, Vienna, 1975

(6)R. Kurz, "Magnet-Inductive Wire Rope Testing" (in German), Draht-Welt, Vol. 51, No. 12, pp. 632-638, 1965

This is a more difficult problem than just the detection and identification of defect type. Accordingly, methods for quantitative characterization are less well developed. However, some previous results are available and are discussed in (2), (6), (7).

- The fourth step is an automated quantitative defect characterization. To make in-line defect characterization possible in wire rope inspection and production processes where large quantities of material have to be inspected often at considerable speed, automated defect characterization schemes have to be implemented. The human operator is no longer capable of handling this time consuming and tedious task. Automated quantitative defect characterization using leakage flux methods is a completely undeveloped area, and no prior work is known. Reported here is a first experimental attempt addressing this problem.

2. THE LEAKAGE FLUX (DC) METHOD FOR WIRE ROPE INSPECTION

The technique used in DC leakage flux testing is to magnetically saturate a section of the steel rope in a longitudinal direction by a strong permanent magnet. Wherever there is an inhomogeneity in the rope such as a broken wire, a broken core, corrosion or abrasion, the magnetic flux is distorted and leaks from the rope into the surrounding air space. Test coils (or sometimes Hall generators) are positioned close to the rope to sense the leakage flux. The rope is moved which causes a changing flux to intersect the coils. The changing flux induces voltages in the coils which are suitably combined and processed to produce the test signals.

(2) M.J.Bergander, "Principles of Magnetic Defectoscopy of Steel Ropes", Wire Journal, pp. 62-67, May 1978

The test signals are usually displayed by a strip chart recorder.

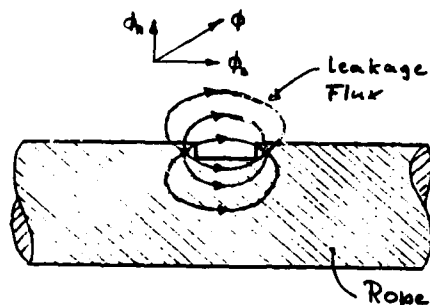


Figure 1: Leakage Flux Due to Rope Flaw

Figure 1 shows a sketch of the magnetic leakage field caused by an inhomogeneity. Figure 2 shows the typical sense coil arrangement for measuring the leakage flux. The sense coil usually has a large number of turns. The coil is subdivided into two halves and hinged. The subdivision is necessary to facilitate mounting the instrument on the rope.

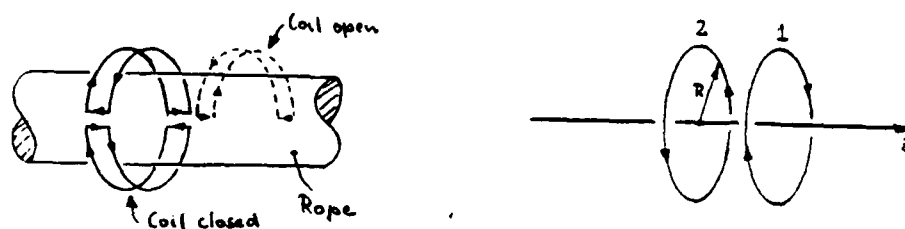


Figure 2: Differential Hinged Sense Coil

3. AUTOMATIC DEFECT CHARACTERIZATION

As borne out by the present research, in implementing an automatic defect characterization scheme using leakage flux methods substantially four distinct signal processing steps are required:

1. Test Signal Generation. Material inhomogeneities in the test specimen cause disturbances of the magnetic leakage field. The changing magnetic field induces the test signal in the sensor.

2. Test Signal Conditioning. To make the test signal useful for the subsequent processing, it usually has to be modified. Pre-amplification is required. Filtering and/or non-linear signal modification are often necessary.

3. Signal Parameter Determination. From a practical viewpoint very few parameters are available to characterize flaw signals, either in the time domain or in the frequency domain. Characteristic parameters are flaw pulse-amplitude and pulsewidth (in the time domain) or signal amplitude and signal frequency (in the frequency domain). Because of the inevitable inaccuracies, caused by noise, a more detailed characterization of the test signal by more than the above parameters does not appear practical at the present time. The signal parameters are extracted from the test signal during this step.

4. Flaw Parameter Computation. The flaw geometry is computed from the signal parameters during this step.

The correspondence between signal parameters and flaw geometry is not unique, i.e. flaws of different shape and location can produce identical signals. To improve the estimate of the flaw geometry, the number of available independent signal parameters can be increased by utilizing an array of sensors. This approach is used in the present study where two concentric coils are used to produce two independent test signals. Figure 3 shows a functional block diagram of a two channel automatic defect characterization scheme.

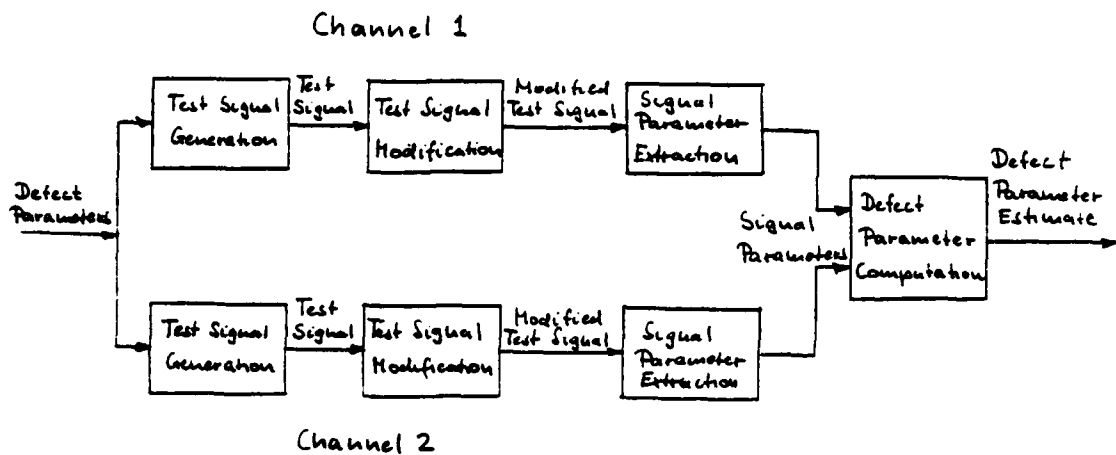


Figure 3: Functional Block Diagram of a Two Channel Automatic Defect Characterization Scheme

4. THE PROPOSED AUTOMATIC DEFECT CHARACTERIZATION METHOD

In electromagnetic wire rope testing by the DC method, the following test parameters influence the waveshape of the test signals:

- a. Magnetic flux density in the rope
- b. Test speed, including direction and continuity of rope movement
- c. Sense coil geometry
- d. Location of the defect in the rope cross section
- e. Defect geometry, including length of defect and magnitude of the change in cross section.

Of these factors, only items d and e characterize the actual rope condition. Parameters a, b, c are unrelated to the rope condition and their influence must be eliminated.

Magnetic flux density in the rope can be held constant by saturating the rope with a permanent magnet of sufficient size.

The influence of test speed, and direction and continuity of the rope movement on the amplitude of the test signal have been eliminated for the NDT Technologies instruments by using proprietary signal conditioning circuitry. This approach will be discussed in the following.

Factors related to the geometry of the defect (see Figure 4) influence the amplitude and the shape of the test signal in a very complicated fashion.

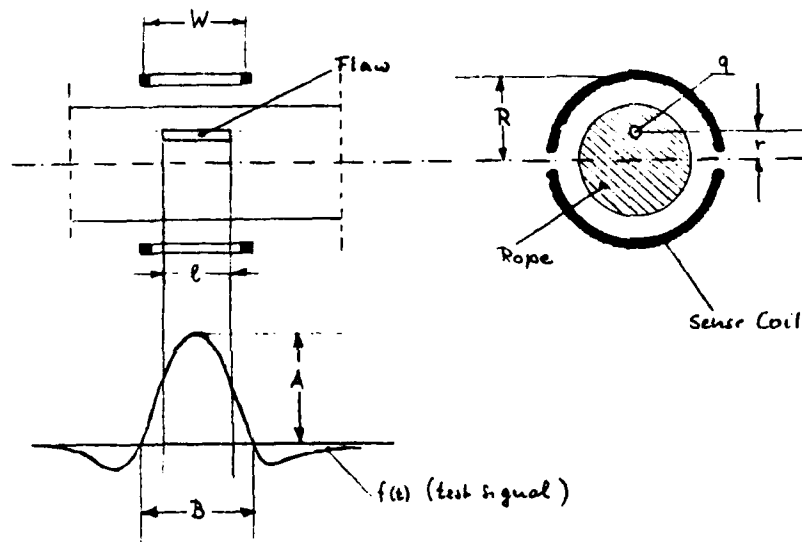


Figure 4: Defect, Coil and Rope Geometry, and Test Signal Waveshape

These factors are: the location of the defect in the rope cross section (the excentricity) r , length of the defect l , and change of cross section caused by the defect q . Other factors which influence the test signal are related to the geometry of the sense coil, such as its radius R and its width W . As a basis for the

proposed automatic defect identification method, a mathematical model relating the flaw parameters to the test signal is required.

An examination of experimental results and of results obtained from the computer simulation (described in Appendix A) suggests that the relationship of parameters in Figure 4 can be represented approximately by the following relationship:

$$A = k \frac{q(1+bl)}{(R-r)^m} \quad (1)$$

where k is a proportionality constant and b , R and m are constants representing the coil geometry. The above equation holds for small values of l ($l < 10\text{mm}$) only. However, this is sufficient since the vast majority of wire breaks have a gap of, at most, only a few millimeters.

Equation (1) can be represented as

$$A = k \frac{A_0}{(R-r)^m} \quad (2)$$

where

$$A_0 = q(1+bl) \quad (3)$$

Note that, independent of coil geometry, A_0 in the above equation depends on the flaw parameters only. It will be called "Fundamental Signal" in the following.

The relationship of Equations (2), (3) holds approximately only for the peak amplitude A of the test signal (see Figure 4) and not for the entire test signal $f(t)$ (t =time). This causes some problems in implementing the automatic defect characterization

scheme which will be discussed below.

Leakage flux testing can detect external and internal rope flaws. However, Equations (2), (3) show clearly the strong attenuation of the flaw signal with increasing distance of the flaw from the sense coil. Therefore, without knowledge of the flaw excentricity it is impossible to relate the flaw signal to the actual loss of rope strength. It is proposed here to find at least a partial solution to this problem by using an array of two or more test coils with different geometries. In particular, the case of two concentric test coils with different diameters is investigated here. This arrangement is shown in Figure 5.

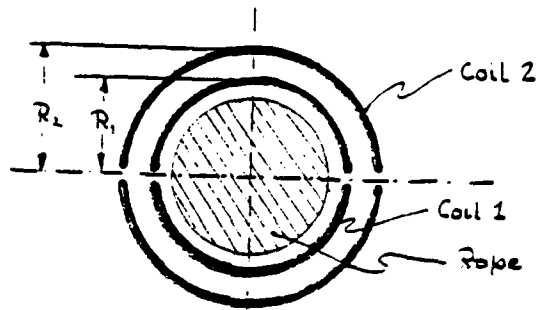


Figure 5: Coil Array

The following relationship holds for the peak amplitudes of the test signals A_1 and A_2 in Coil 1 and 2, respectively.

$$A_1 = k_1 \frac{A_0}{(R_1 - r)^m} \quad (4)$$

$$A_2 = k_2 \frac{A_0}{(R_2 - r)^m} \quad (5)$$

According to the above discussion, the Fundamental Signal A_0 depends on the flaw parameters only and is independent of flaw location and test coil geometry.

From (4) and (5), A_o and r can be determined

$$\frac{\Delta r}{\Delta R} = \frac{\left(k \frac{A_1}{A_2}\right)^{\frac{1}{m}}}{1 - \left(k \frac{A_2}{A_1}\right)^{\frac{1}{m}}} \quad (6)$$

$$A_o = A_1 (\Delta r)^m \quad (7)$$

where

$$\Delta r = R_1 - r \quad (\text{the distance of the flaw from the inner coil})$$

$$\Delta R = R_2 - R_1 \quad (\text{the distance between the two sense coils})$$

The mathematical model of Equations (6), (7) has two adjustable parameters k and m which, within the experimental accuracy limitations, allows fairly accurate curve fitting. One of the major advantages of choosing a mathematical model of the form (4), (5) is its easy real time realization with rather simple analog circuitry. So-called "Multifunction Converters" are readily available in integrated circuit form, and can be conveniently used to implement Equations (6) and (7).

The implementation and evaluation of an automated defect characterization scheme for the inspection of wire rope in accordance with Figure 3 will now be discussed in more detail.

4.1 Sensor Design

Figure 1 shows a sketch of the magnetic leakage field caused by an inhomogeneity. Note that the rope is saturated and the actual shape of the leakage field caused by the flaw is not well understood. However, a comparison of experimental results with results obtained from the computer simulation suggests that the leakage field caused by a gap, such as a broken wire, indeed resembles the field of a magnetic dipole as shown in Figure 1. Note, however, that the equivalent dipole distance is bigger than the gap width, especially for narrow gaps.

Figure 2 shows the typical sense coil arrangement for measuring the radial component ϕ_R of the leakage flux. The sense coil usually has a large number of turns. It is subdivided into two halves and hinged. This subdivision is considered necessary to facilitate mounting the instrument on the rope.

The hinged arrangement shown in Figure 2 is equivalent to the idealized coil arrangement which is shown in the same figure. As these coils move along the z-axis, voltages are induced by the changing flux caused by magnetic inhomogeneities. Most instruments have a differential coil arrangement as shown in Figure 2 and use the induced voltages as a test signal. In this case, however, test signal amplitudes are directly proportional to rope speed. For an automatic flaw identification scheme, this is not acceptable.

To remedy this problem and to make the test signal independent of rope speed, an arrangement as shown in Figure 6 with two hinged coils side-by-side is used. The induced signals from both hinged coils are subtracted and the difference is integrated. The ampli-

tude of the integrated difference signal is then independent of speed, and its waveshape is substantially identical to the waveshape obtained from the single hinged coil arrangement. This can be demonstrated as follows.

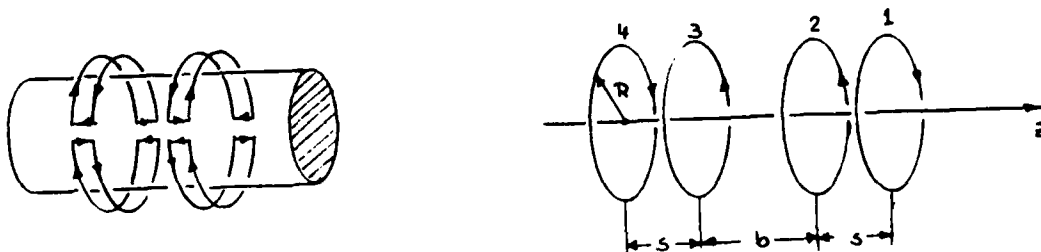


Figure 6: Double Differential Hinged Coil Arrangement

Assume the coils in Figure 2 move in the z -direction at some speed v , and let the total flux in Coil 1 (as a function of its instantaneous position z) be $\phi(z)$. Then the total magnetic flux linkage $\Psi(z)$ in Coils 1 and 2 is

$$\Psi(z) = \phi(z) - \phi(z-s) \quad (8)$$

Since z is a function of time we have the time derivative

$$\dot{\Psi}(z) = v \Psi_z(z) \quad (9)$$

where

$$v \triangleq \frac{dz}{dt}$$

$$\Psi_z(z) \triangleq \frac{d}{dz} \Psi(z)$$

The test signal voltage induced in Coils 1, 2 is proportional to $\dot{\Psi}(z)$. Hence, according to (9), the test signal obtained from these coils is proportional to speed. Furthermore its polarity

depends on the direction of rope movement.

Now consider the four-coil arrangement of Figure 6. Its total magnetic flux linkage is

$$\Psi_4(z) = \Psi(z) - \Psi(z-s-b)$$

Since

$$\Psi_z(z) = \lim_{(s+b) \rightarrow 0} \left(\frac{\Psi_4(z)}{(s+b)} \right) ,$$

$$\Psi_z(z) \approx \frac{\Psi_4(z)}{(s+b)} \quad \text{for } (s+b) \text{ sufficiently small}$$

$\Psi_4(z)$ can be easily obtained by integrating the combined induced voltages of Coils 1-4. Hence, the integrated voltages induced in the coils as shown in Figure 6 are indeed equivalent to the voltages induced in the coil arrangement shown in Figure 2 and independent of speed.

4.1.2 Design Criteria

For the sense coil design the following design criteria have to be considered:

1. Resolution. The resolution of a transducer is measured by the smallest distance between flaws for which the transducer provides distinctly separate flaw indications.
2. Signal-to-Noise Ratio. The only signals of interest in non-destructive testing are flaw related signals. Any signals that are not flaw related must be considered noise. In nondestructive rope testing the noise is primarily caused by the nonhomogeneous rope

structure (i.e. test specimen noise). Structure related noise signals will be referred to as "Intrinsic Noise" in the following. The intrinsic noise causes serious problems, and it makes test signals always very noisy. As compared to the intrinsic noise, noise caused by other sources (e.g. system noise) is insignificant and can be neglected.

3. Sensitivity. The sensitivity of a sensor is measured as the signal amplitude caused by a predetermined flaw. The sensitivity of a sense coil is primarily determined by the number of turns and by the coil width.

4. Repeatability. Since the sense coil is subdivided, it is no longer point symmetric. Hence noise as well as flaw signals depend on the azimuthal position of the rope with respect to the sense coil, and complete repeatability of signals cannot be assured. This problem will be discussed further in Chapter 5.4.

In optimizing the above design criteria, only sensitivity does not cause any problems. Sensitivity can easily be increased by increasing the gain of the preamplifier and/or the number of turns of the sense coil. However, resolution and SNR cannot be simultaneously optimized for one set of coil parameters, and the best possible compromise has to be found.

A good measure of resolution is the pulsewidth B of the flaw signal (see Figure 4). I.e., to achieve maximum resolution, the flaw signals have to be as narrow as possible.

The intrinsic noise is primarily caused by the subdivided and hinged sense coil (see Figures 2 and 6) together with the nonhomogeneous rope structure. A steel wire rope is an arrangement of separate wires wound in a helical shape to form strands. The strands are then laid together in a helix to form the rope. The strands cause a leakage field parallel to the strands as shown in

Figure 7. This field has been experimentally verified (8).

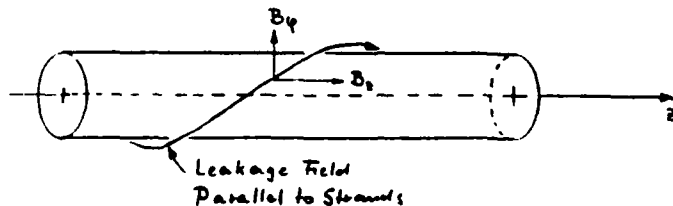


Figure 7: Azimuthal Leakage Field

Obviously then, the flux surrounding the rope has an axial component B_z and an azimuthal component B_ϕ . Since the search coil is subdivided as shown in Figure 6, the azimuthal field component induces an intrinsic noise voltage in the search coil as the rope moves.

Equation 1 shows the strong dependence of the amplitude of flaw related pulses on the location of the flaw within the rope (its eccentricity r). Hence, since the intrinsic noise signal is primarily caused by the inhomogeneous rope surface, it can cover up signals caused by interior flaws to such an extent that they can no longer be detected. Because of this, the amplitude ratio α has to be maximized for an optimum SNR. Here, α is defined as the ratio of the signal amplitude caused by an internal flaw to signal amplitude caused by an identical surface flaw.

The above observations are illustrated in Figure 8 which shows the amplitude ratio α and flaw signal pulsewidth B as a function of

(8)U.B.Meyer, "Electromagnetic Testing of Wire Ropes" (in German), Mitteilungen aus dem Institut fuer Elektrische Maschinen an der ETH, Professor A.Dutoit, Editor, Juris Druck und Verlag, Zuerich, 1973

coil width s and coil Radius R . These data were obtained from the coil simulation program.

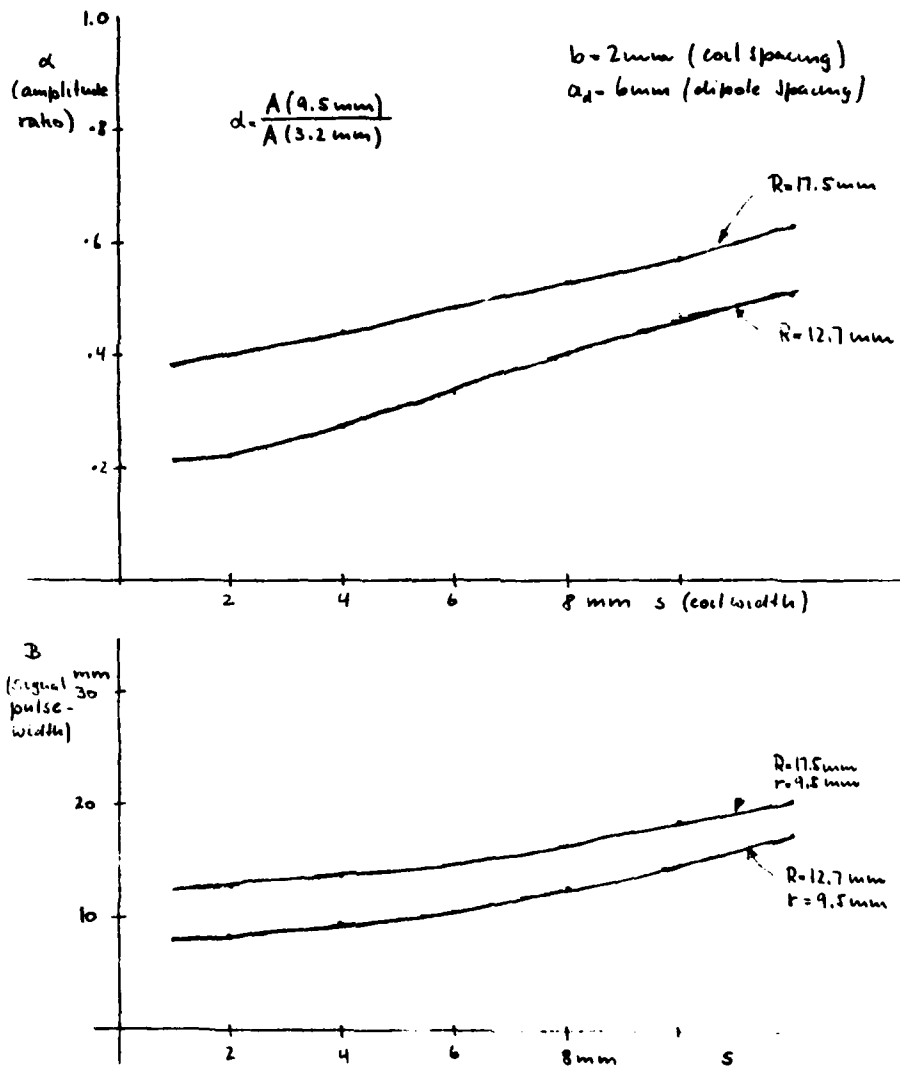


Figure 8: Amplitude Ratio and Flaw Signal Pulsewidth B

An inspection of this figure shows that, for any coil, the ampli-

tude ratio α (and hence the SNR) cannot be maximized while at the same time the pulsewidth B is minimized (i.e. resolution is maximized).

For the implementation of an automatic defect identification scheme, using Equations (4), (5), it is desirable to have the first coil with the smallest possible amplitude ratio α_1 , and the second coil with largest feasible amplitude ratio α_2 . This will minimize the effects of measurement errors in A_1 and A_2 on the computed value of Δr in Equation (6). To make this statement plausible, assume that both coils have identical amplitude ratios α . Then Equations (4), (5) are no longer independent and Equation (6) can not be used to determine Δr . A further discussion of this subject is beyond the scope of the present report.

In accordance with the above considerations, a sense head with the following coil parameters was designed and built:

Coil #1: $s = 2\text{mm}$, $b = 2\text{mm}$, $R = 12.7\text{mm}$ (i.e. $\alpha_1 = 0.22$)

Coil #2: $s = 2\text{mm}$, $b = 2\text{mm}$, $R = 17.5\text{mm}$ (i.e. $\alpha_2 = 0.40$)

Figure 9 (see also Figure 11) shows test results obtained from these coils. Note that, as discussed above Coil #1 shows better resolution and is better suited for detecting small surface flaws. However, the intrinsic noise is very pronounced in the Coil #1 signal. Coil #2 offers a better SNR. However, it has lower resolution and it is not as well suited for detecting relatively small surface flaws.

Figure 9 shows the normalized signal amplitudes $a(r)$ for Coil #1 and Coil #2 for the equivalent of a 3/4" rope. Results from the computer simulation (see Appendix) and experimental results are shown. Because of the difficulty in preparing a test rope with well

defined external and internal flaws, the experimental results were obtained from five concentrically arranged tubes with well defined holes. (Specifications for these test tubes are given in Table 1).

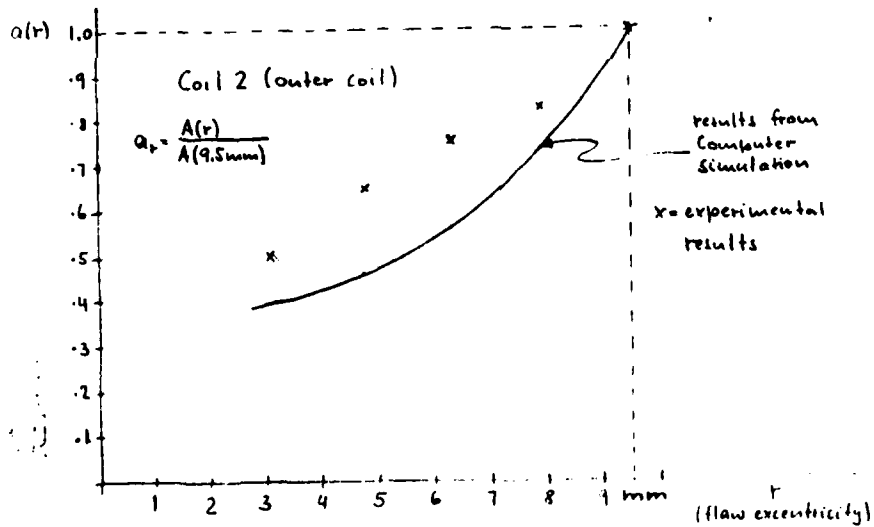
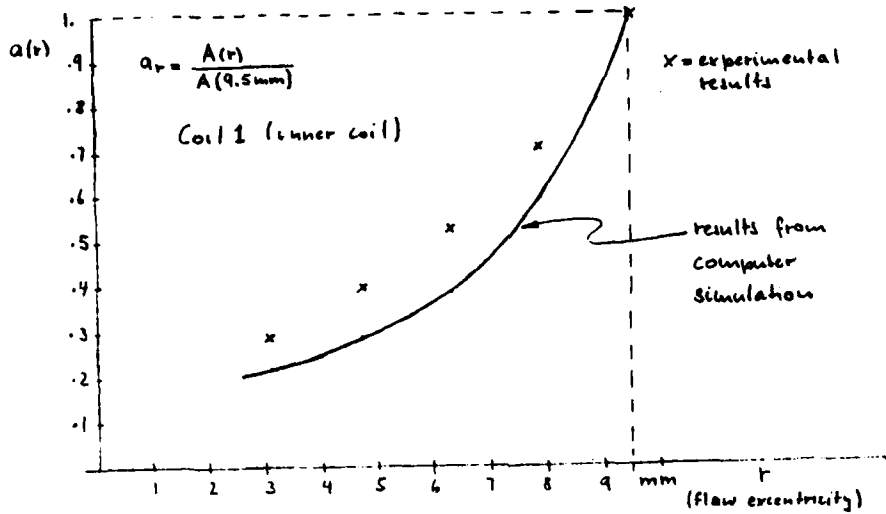


Figure 9: Normalized Flux Signal Amplitudes as a Function of Flux Excentricity

The experimental results were obtained from Figure 10.

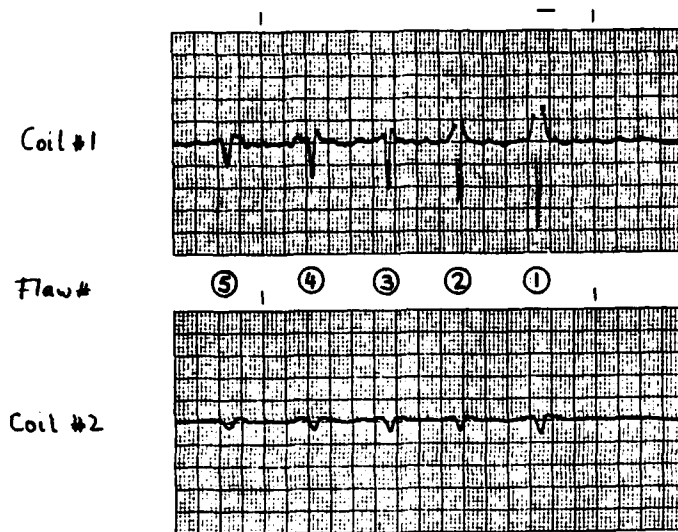


Figure 10: Experimental Results from 3/4" Concentric Test Tubes

Figure 11 gives also a comparison between results from the experimental prototype unit, built for the present project, and results obtained from one of the Canadian instruments. It shows that the performance of the prototype coils compare favorably with competing instruments.

4.2 Test Signal Conditioning

A complete functional block diagram of the automatic defect identification scheme is shown in Figure 12. Frequent reference will be made to this block diagram in the following. As a first step in signal conditioning, signal amplification and integration are required. This was discussed in the previous chapter. In Figure 12 the preconditioned signals are called $f_1(t)$ and $f_2(t)$, respectively. The preconditioned signals from Coil #1 and Coil #2 cannot be

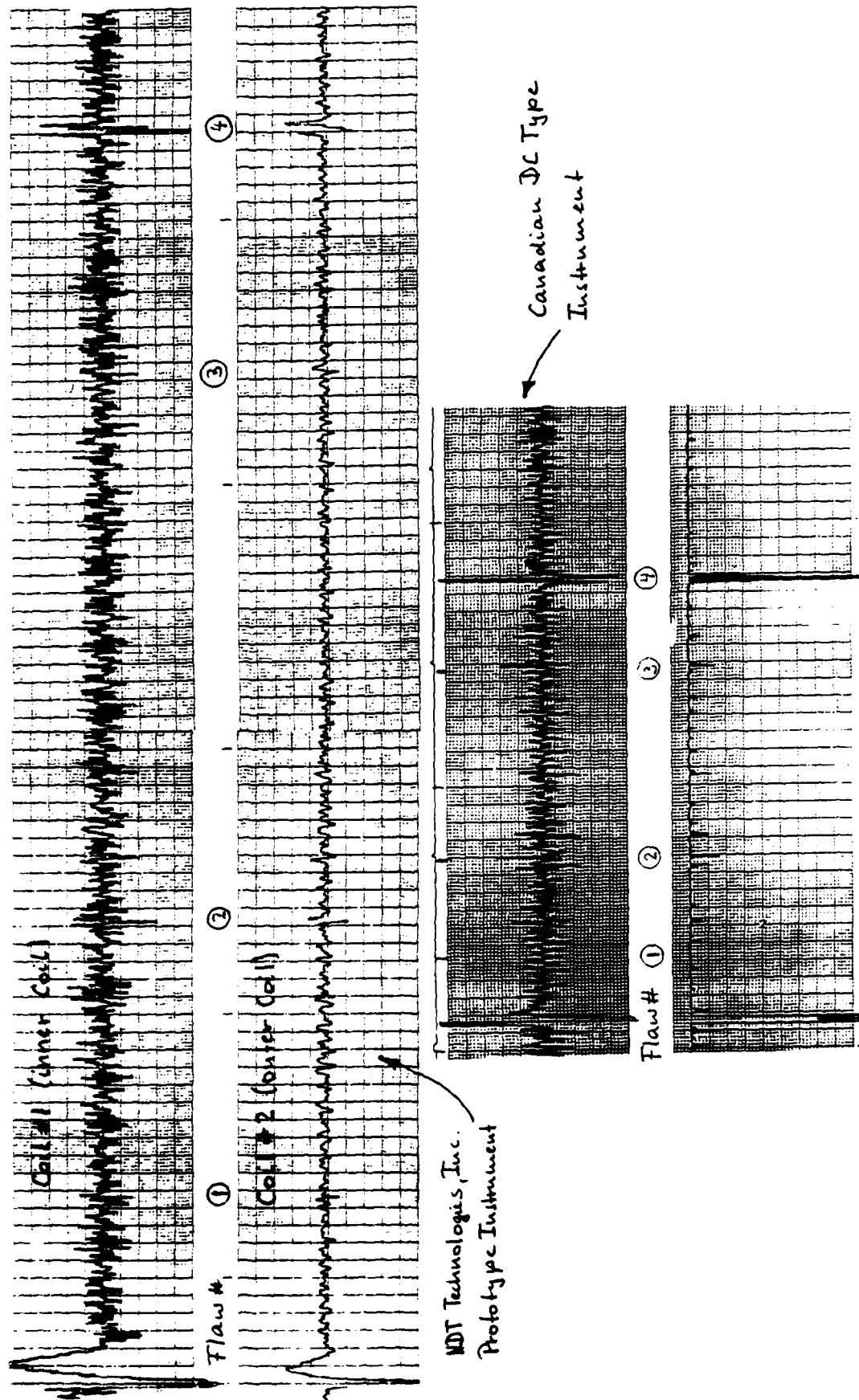


Figure 11: Comparative Strip Chart Recordings of Prototype Instrument and from Another DC-Type Rope Tester Instrument

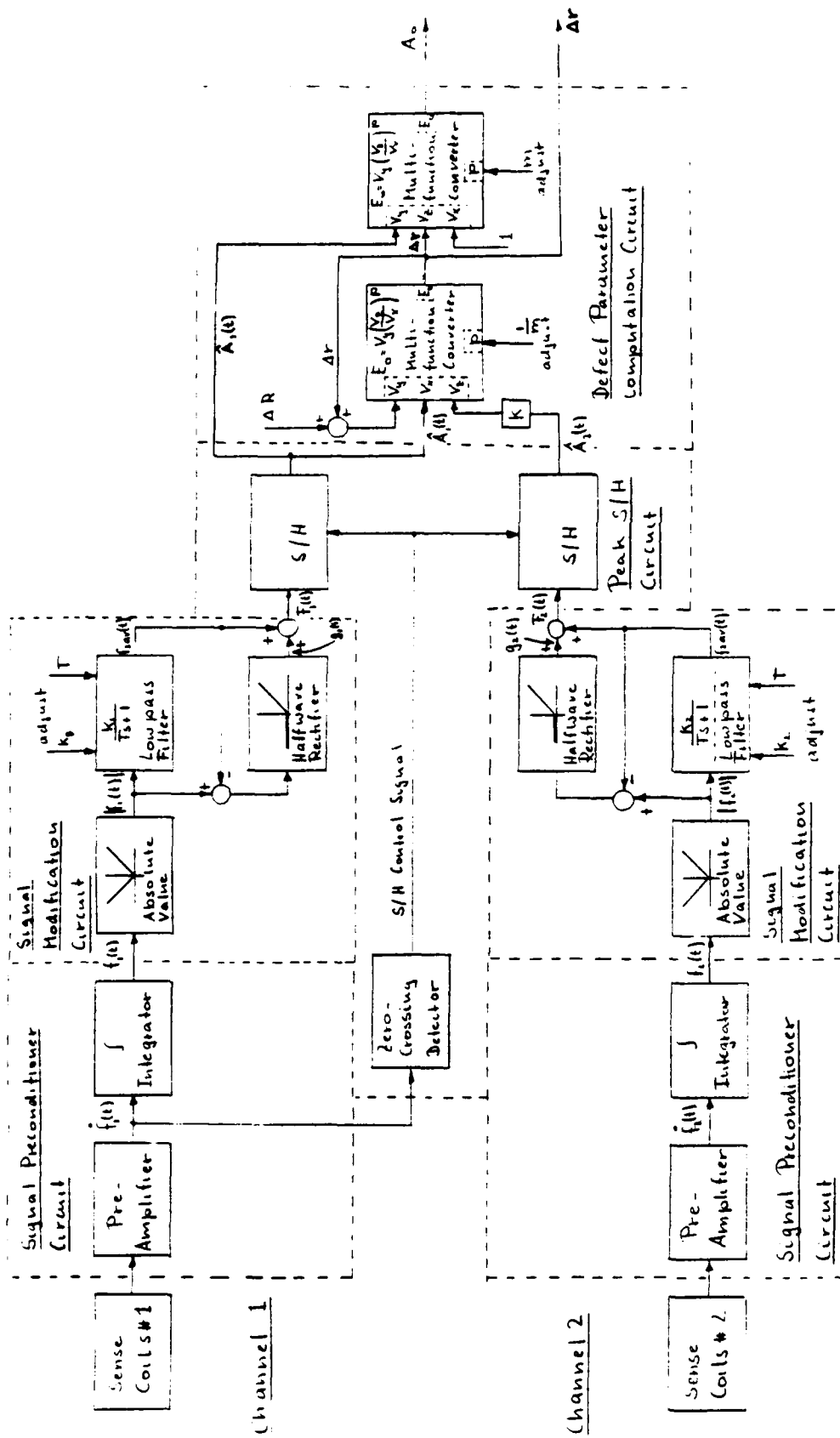


Figure 12: Functional Block Diagram of Automatic Defect Identification Scheme

used directly to compute the flaw excentricity r and the Fundamental signal A_0 from Equations (6), (7). This becomes immediately clear by examining the waveshapes of both test signals as shown in Figure 10 (see also Figure 28 of Appendix A). Signals $f_1(t)$ and $f_2(t)$ do not have identical waveshapes, and using them directly as input for Equation (6) would yield correct results only for the peak values A_1 and A_2 of $f_1(t)$ and $f_2(t)$. For all other time instants the results would be grossly erroneous. For instance, Equation (6) is meaningless for $A_1 = f_1(t) < kf_2(t) = kA_2$ a condition which occurs quite frequently (cf. Figure 10).

Two signal conditioning steps are used to remedy this situation.

4.2.1 Test Signal Modification

As part of Figure 12 a functional block diagram of the first signal conditioning stage is shown which will be called Signal Modification Circuit in the following

Transfer characteristics of this circuit are

$$\begin{aligned} F(t) &= |f(t)| && \text{if } |f(t)| > kf_{av}(t) \\ F(t) &= kf_{av}(t) && \text{if } |f(t)| \leq kf_{av}(t) \end{aligned} \quad (10)$$

where $F(t)$ is the output signal, $f(t)$ is the input signal and $f_{av}(t)$ is an average value of $f(t)$ obtained by fullwave rectification and low-pass filtering. $f_{av}(t)$ is sometimes called the mean-absolute-deviation (MAD) value. k is a proportionality constant determining the signal level above which localized flaws are detected. The operation of the Signal Modification Circuit is easily understood by considering that in both channels (cf. Figure12)

$$\begin{aligned} g(t) &= |f(t)| - f_{av}(t) && \text{if } |f(t)| > kf_{av}(t) \\ g(t) &= 0 && \text{if } |f(t)| \leq kf_{av}(t) \end{aligned} \quad (11)$$

Substantially, the Signal Modification Circuit leaves the peak values of $f(t)$ unchanged and replaces the rest of $f(t)$ by its weighted average value. Typically k is adjusted such that $kf_{av}(t)$ is slightly above the peak values of the signal noise.

For a number of experiments the transfer characteristics of the Signal Modification Circuit was changed to

$$\begin{aligned} F(t) &= |f(t)| & \text{if } |f(t)| > L \\ f(t) &= L & \text{if } |f(t)| \leq L \end{aligned} \quad (12)$$

where L is a constant signal level which can be externally adjusted to some suitable value.

Note that the Signal Modification Circuit retains all the information contained in the test signal that is essential for test signal interpretation, while discarding the unimportant part of the signal. Because of this, for the interpretation by the human operator, the signal interface signal has some significant advantages:

- In the visual display of the test signal, flaw pulses are highlighted and the noise signal is suppressed. This type of signal modification has been called "display cosmetics". Display cosmetics is often helpful, especially when very long ropes with extensive strip chart recordings have to be evaluated, sometimes on-site.
- A measure for a quantitative assessment of the signal noise is available. A change in noise amplitude usually indicates a continuous flaw such as corrosion and/or abrasion. It can be conjectured that, by using the functional relationship (6), (7), together with the Signal Modification Circuit, it is possible to diagnose internal corrosion and abrasion as well.

Based on the above observations, the signal modification circuit is a simple and valuable diagnostic tool. It is worth using even in low cost and simplified rope test instruments.

Two Signal Modification Circuits are required for processing of signals from Coil #1 and Coil #2, respectively.

The outputs of the Signal Modification Circuit, however, are still not suitable for the computation of Δr and A_0 according to Equations (6), (7). These equations hold strictly for the peak values

of $A_1(t)$ and $A_2(t)$, and the ratio $\frac{A_2(t)}{A_1(t)}$ differs considerably from the ratio of peak values $\frac{A_2}{A_1}$. This, in turn, distorts the computed Δr and A_0 signals to such an extent to make them useless.

4.2.2 Peak Sample/Hold Circuit

To remedy the above situation, a peak sample/hold circuit was designed and built.

As part of Figure 12, a functional block diagram of the Peak S/H circuit is shown. Its basic function is to sample the (positive and negative) peaks of the test signal and to hold their value until the next peak value is sampled, and so on.

The operational principles of the Peak Sample/Hold circuit are very simple. The circuit samples whenever the time derivative of the input signal becomes zero. At all other times, it holds the sampled value. Note that the signal which is sampled can be any signal, such as the input signal itself or the input signal modified by the previously mentioned Signal Modification Circuit.

In the functional block diagram of Figure 12 the derivative of the test signal $\dot{f}(t)$ is readily available and can be used to generate the S/H control signal. The zero-crossing detector produces a short logic-high pulse whenever the differentiated input signal crosses zero, i.e. whenever the time derivative of the test signal $f(t)$ is zero. The logic signal controls the operating mode of a commercially available sample and hold amplifier (such as Signetics NE 5537 or equivalent). The S/H amplifier is in the sample mode whenever the (logic) control signal is (logic) high, and in the hold mode if the control signal is (logic) low.

The peak sample and hold operation is a very crucial step in implementing an automatic defect characterization scheme. It allows an exact identification of signal peaks as required for further signal processing according to Equations (6), (7). Furthermore, it allows mathematical operations on the test signal in a time frame which is expedient.

In the functional block diagram of Figure 12, sampling is controlled by Signal Channel 1, i.e. $F_1(t)$ and $F_2(t)$ are sampled whenever $f_1(t) = 0$. This approach was used in the actual circuit implementation.

Some other sampling strategies are also possible. For instance $F_1(t)$ could be sampled whenever $\dot{f}_1(t) = 0$ and $\dot{f}_2(t) = 0$. Another strategy would be to sample $F_1(t)$ if $f_1(t) = 0$ and to sample $F_2(t)$ if $f_2(t) = 0$.

The Peak Sample/Hold Circuit accomplishes the function of parameter extraction. It determines peak values of the test signal and it holds them for further processing by the following computation circuit.

4.2.3. Defect Parameter Computation Circuit

The block diagram of the Defect Parameter Computation Circuit is shown as part of Figure 12. Mathematically, this circuit transforms the signal parameters A_1 and A_2 into the flaw parameters Δr and A_0 according to Equations (6), (7). The operation of this circuit is easy to understand by considering that Equation (6) can be represented as

$$\Delta r = \left(\frac{A_2}{A_1} \right)^{\frac{1}{3}} (\Delta R + \Delta r)$$

The block diagram in Figure 12 is a direct realization of this equation. The circuit itself has a very low parts count. It requires only two multifunction converters such as the National Semiconductor LH0094 or equivalent. These devices are readily available in integrated circuit form.

5. EXPERIMENTAL RESULTS

5.1 Hardware Implementation

Implementations of the Signal Modification Circuit, the Peak Sample/Hold Circuit, and the Flaw Computation Circuit are shown in Figure 13, Figure 14, and Figure 15, respectively. The Circuit diagrams are direct realizations of the functional block diagram of Figure 12. They are self-explanatory. A circuit diagram of the Signal Preconditioner Circuit is not shown.

A prototype instrument for testing ropes up to 1 3/4" diameter was built for this project. Figure 16 shows the prototype and Figure 17 shows an alternate prototype of instrument implementations of the proposed approach. Figure 18 (foreground) shows the two coil sense head used in the experiments. An additional sense head without hinges was also designed and built. In this case, the two coil halves are connected by connectors which would

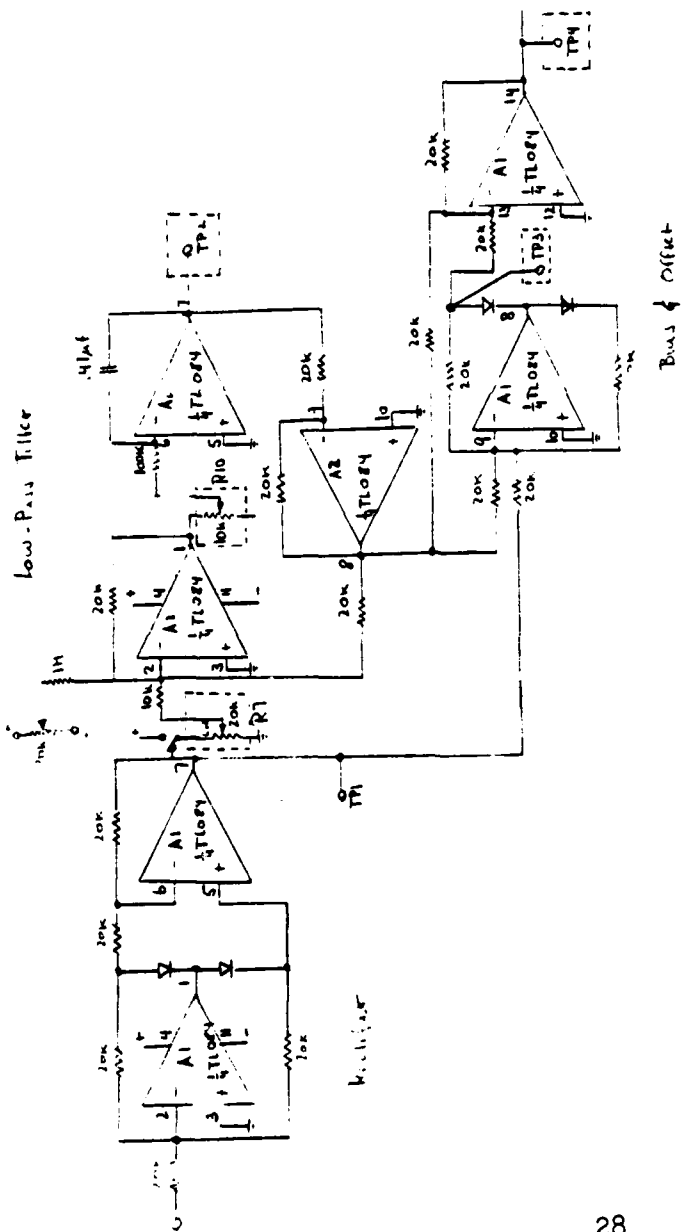
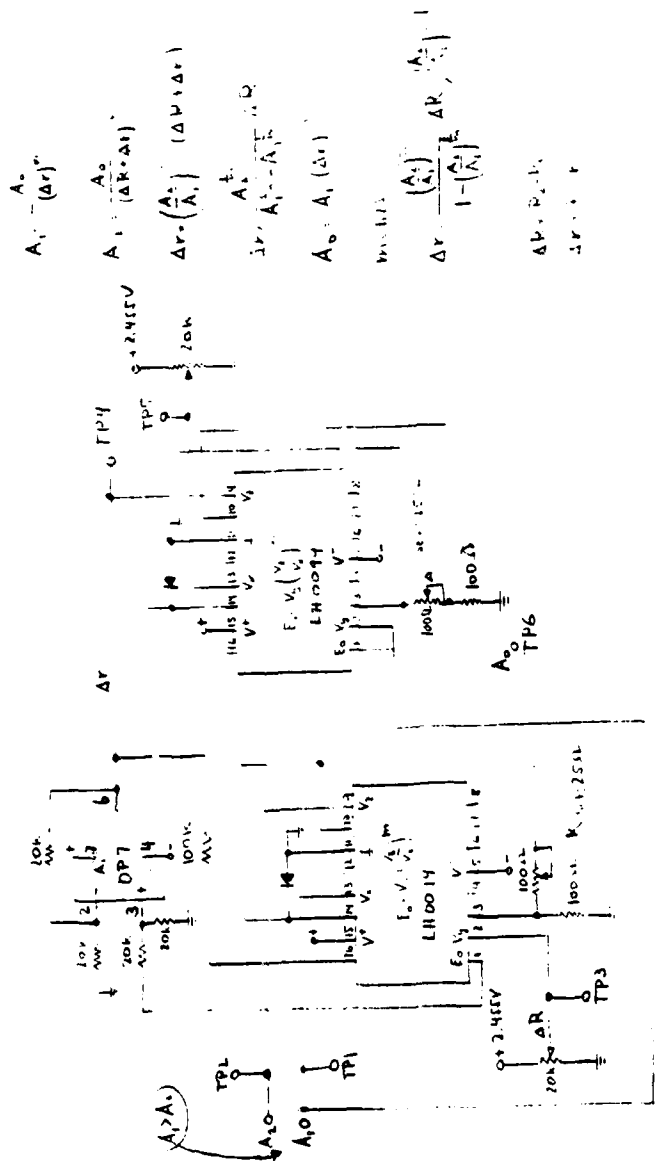


Figure 13: Signal Modification Circuit



$$A_{11} = \frac{A_0}{(\Delta r)^2}$$

$$A_{10} = \frac{A_0}{(\Delta R \cdot \Delta r)}$$

$$\Delta r = \left(\frac{A_0}{A_1} \right) (\Delta R + \Delta r)$$

$$A_{10} = A_1 (\Delta r)$$

$$\Delta r = \frac{A_0}{1 - \left(\frac{A_0}{A_1} \right) \Delta R}$$

$$\Delta R = R_0 - R_1$$

$$\Delta r = r_0 - r_1$$

Figure 15: Defect Parameter Computation Circuit

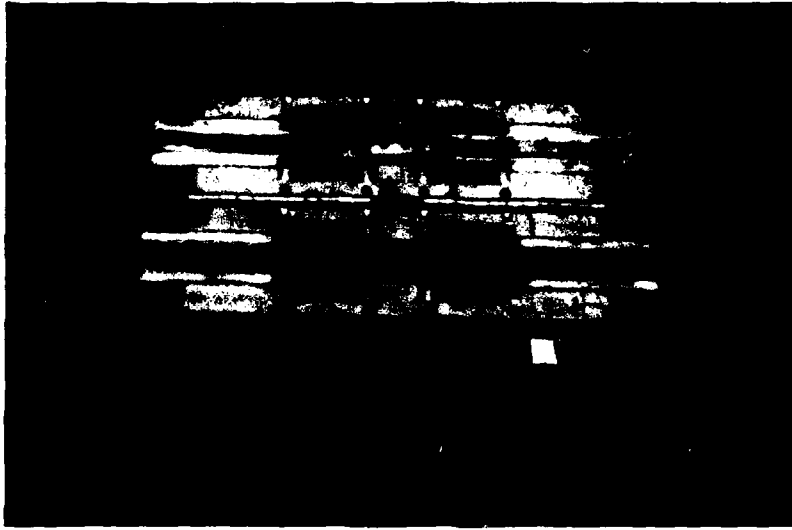


Figure 16: Prototype Rope Tester

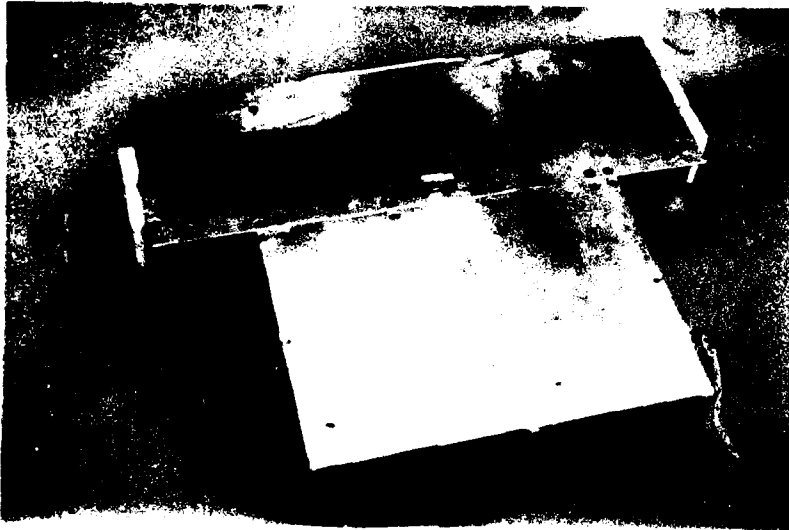


Figure 17: Alternate Prototype

avoid the above mentioned problems associated with the divided and hinged coil design. The alternate pickup head is shown in Figure 18 (background). Its design requires a preamplifier with a very high gain, which caused considerable noise problems. Therefore this design was discarded.

A test rig, as shown in Figure 19, was constructed to permit dynamic testing of the prototype . The wheels of the test rig support a continuous loop of steel wire rope. One wheel is driven by a variable speed DC drive. The testing speed is adjustable up to 500 ft/min.

Several tests were conducted to demonstrate the feasibility of the proposed automatic defect characterization method.

5.2 Experimental Results from a Rope Model

As pointed out above, leakage flux tests are indirect. That is, they respond to variables not necessarily directly related to in service performance of the wire rope. Placing them on a quantitative basis is a challenging objective. For instance, it is very difficult to manufacture test ropes with well defined external and internal artificial flaws. Therefore, in order to evaluate the proposed method under closely controlled conditions, a rope model was manufactured. Five concentric steel tubes were used. To simulate rope flaws, identical holes with 1.6mm (0.0675 inch) diameter were drilled into each tube. The wall thickness of each tube is 0.89 mm (0.035"). The outer tube diameters were respectively 19 mm, 15.8 mm, 12.7 mm and 6.4 mm (0.75", 0.625", 0.5", 0.375", 0.25" respectively). With these dimensions, the test specimen of concentric tubes has a fill factor of 0.577, similar to the fill factor of most IWRC ropes.

The parameters m and k in Equations (6), (7) were experimentally determined: $m = 1.25$, $k = 2$. Figure 20 shows a plot of Equation (6)

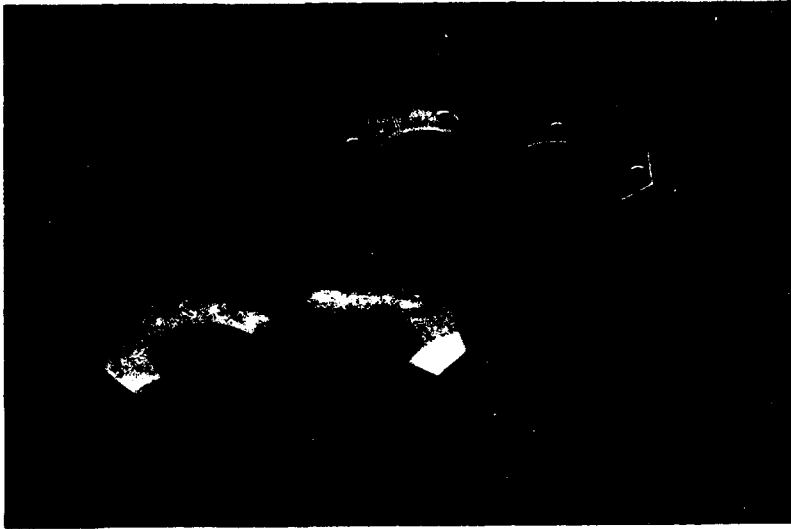


Figure 18: Experimental Sense Heads



Figure 19: Wire Rope Test Rig

with these parameters as compared to experimental results. Also shown in the figure is an alternative approximation with a different set of parameters (i.e. $m = 1.38$, $k = 1.92$) which shows the great flexibility of the multifunction converter in function approximation.

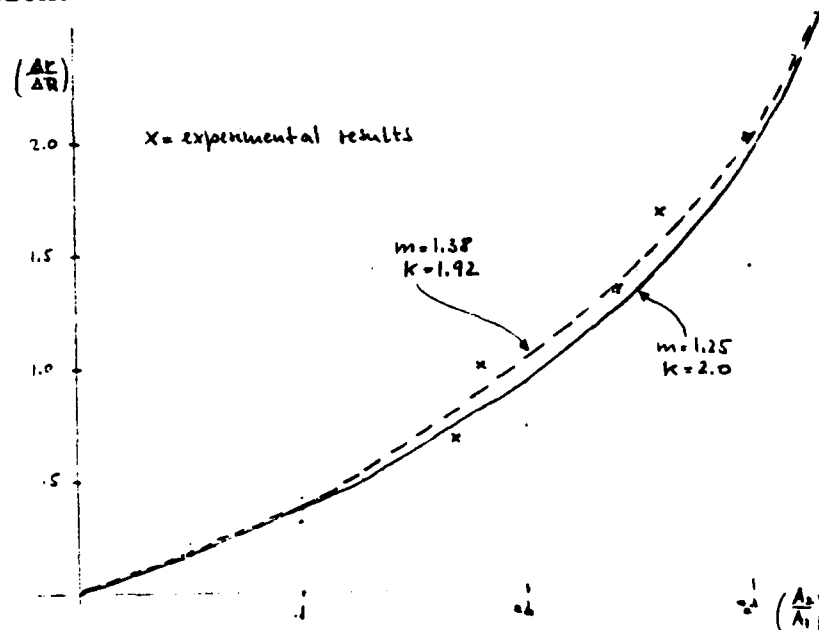
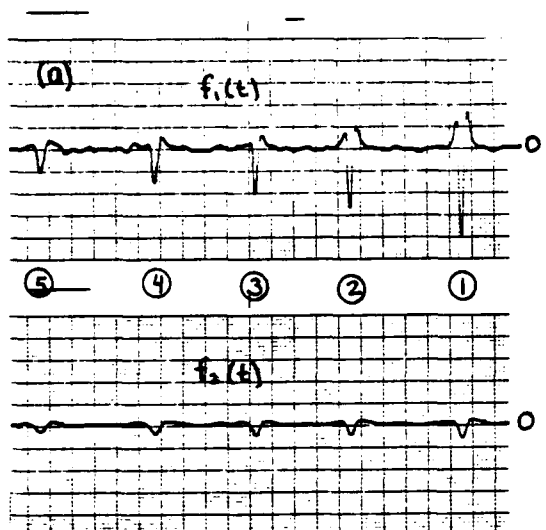
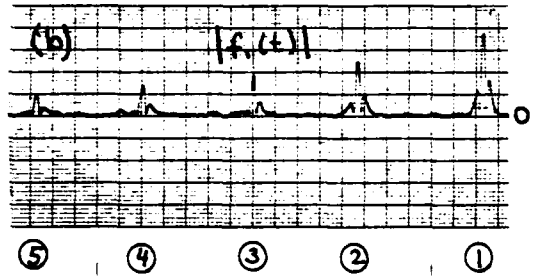


Figure 20: Function Approximation of Defect Parameter Computation Circuit (Equation 6)

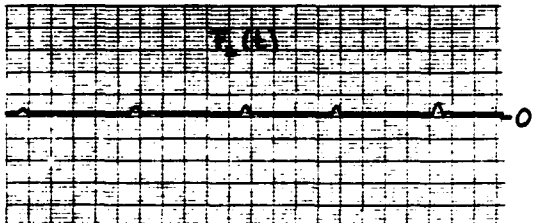
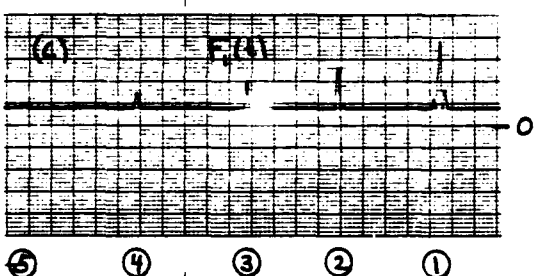
For easy reference flow parameters are repeated in Table 1. Actual test results are shown in Figure 21. Figure 21 a shows $f_1(t)$ and $f_2(t)$, respectively, the unmodified test signals (cf. Figure 12). $|f_1(t)|$ and $|f_2(t)|$, the rectified test signals, are shown in Figure 21b. In Figure 26c, $F_1(t)$ and $F_2(t)$, the modified test signals are shown. Note that the input output characteristics of the signal modification circuit is that of Equation 12. Figure 21d shows $\hat{A}_1(t)$ and $k\hat{A}_2(t)$, the modified test signals $F_1(t)$ and $F_2(t)$ after the peak-sample-and-hold operation. Figure 21e shows the normalized defect distance $\frac{\Delta r}{\Delta R}$ and the amplitude A_0 of the Fundamental Signal.



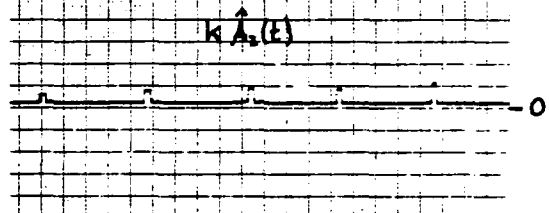
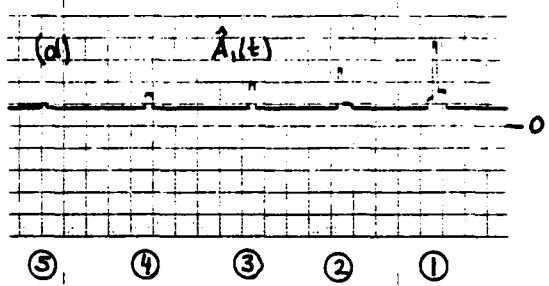
Preconditioned Signals



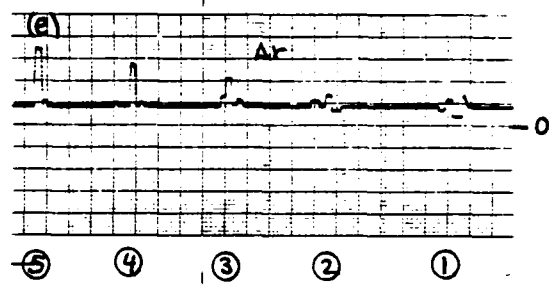
Preconditioned Signals (Abs. Value)



Modified Signals



Modified & Peak-Sampled Signals



Computed Defect Parameter Signals

Figure 21;
Test Results obtained from
Concentric Test Tubes

In Table 1 the major experimental results are tabulated. The measurement of $\frac{\Delta r}{\Delta R}$ shows a systematic error which could have been eliminated by a more careful determination of k and m. (The lack of time combined with a breakdown of the stripchart recorder precluded further experimentation.) The measured fundamental signal amplitude A_o is shown normalized with respect to the average A_{oav} of the 5 measured values.

Flaw #	r(mm)	Δr (mm)	$\left(\frac{\Delta r}{\Delta R}\right)$ actual	$\left(\frac{\Delta r}{\Delta R}\right)$ measured	$\left(\frac{\Delta r}{\Delta R}\right)$ error	$\left(\frac{A_o}{A_{oav}}\right)$ actual	$\left(\frac{A_o}{A_{oav}}\right)$ measured
①	9.5	3.2	0.67	0.6	-10%	1	1.00
②	7.9	4.8	1.00	0.7	-30%	1	0.82
③	6.4	6.4	1.33	1.05	-21%	1	1.07
④	4.8	7.9	1.67	1.40	-16%	1	1.10
⑤	3.2	9.5	2.00	1.7	-15%	1	1.00

Table 1

Flaw ② shows a relatively large discrepancy between measured and actual values. A visual inspection indicates that this tube is probably made from a different type of steel. There are other potential error sources. Wire ropes are usually oversized. Hence the rope guides have to be oversized which introduces excentricity as to the actual position of the test steel tubes with respect to the sense coils. Another error source is the subdivision of the hinged sense coils which makes flaw pulses dependent on the angular position of the steel tubes. This problem will be discussed in slightly more detail in the next chapter.

5.3 Experimental Results from a Test Rope

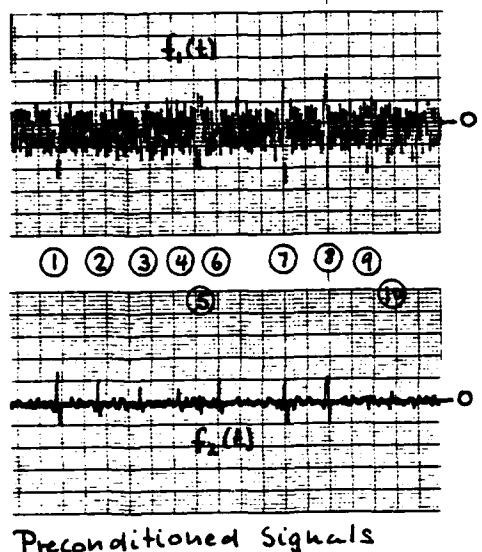
Further experiments were conducted with a test rope (3/4", 6x19 IRWC rope). Several short pieces of wire were inserted into this rope to simulate internal flaws. One crown wire was cut to simulate a rather small external flaw. The following is a list of flaws:

- ① 0.047" dia. wire, 5/8" long laid into groove between strands
- ② 0.047" dia. wire, 1/4" long laid into groove between strands
- ③ 0.047" dia. wire, 1/8" long laid into groove between strands
- ④ 0.047" dia. wire, 1/8" long pushed under strands
- ⑤ unknown flaw, possibly internal wire, welded during manufacture
- ⑥ 0.047" dia. wire, 1/4" long pushed under strands
- ⑦ 0.047" dia. wire, 5/8" long pushed under strands
- ⑧ 0.047" dia. wire, 1" long pushed under strands
- ⑨ 0.047" dia. wire, gap width approximately 0.040", cut on crown
- ⑩ unknown flaw, possibly internal wire, welded during manufacture

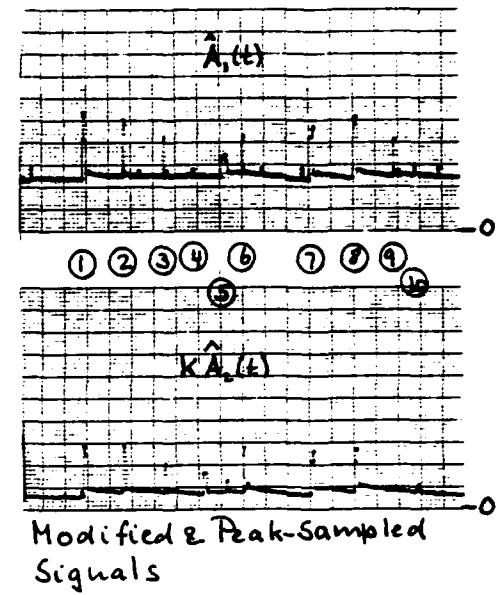
Since it is difficult to produce test ropes with well defined artificial flaws, these test results can only be evaluated in a semi-quantitative fashion.

Figure 22 and Figure 23 show results obtained from the above described test rope. Two different signal modification circuits were used. Figure 22 was obtained by using the transfer characteristic (10) and Figure 23 shows results which were obtained by using a signal modification circuit with transfer characteristic (12).

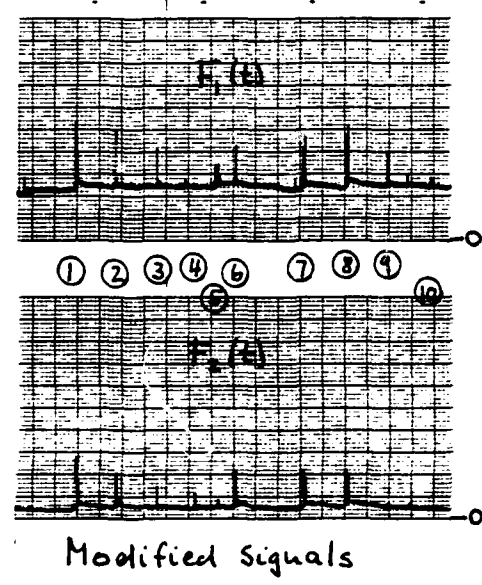
In both figures, Flaw ③ and Flaw ④ have identical geometries therefore they have approximately identical Fundamental Flaw Signal amplitudes A_0 , as shown. The flaw distance Δr is greater for Flaw ④ than for Flaw ③, which is clearly indicated in the figures.



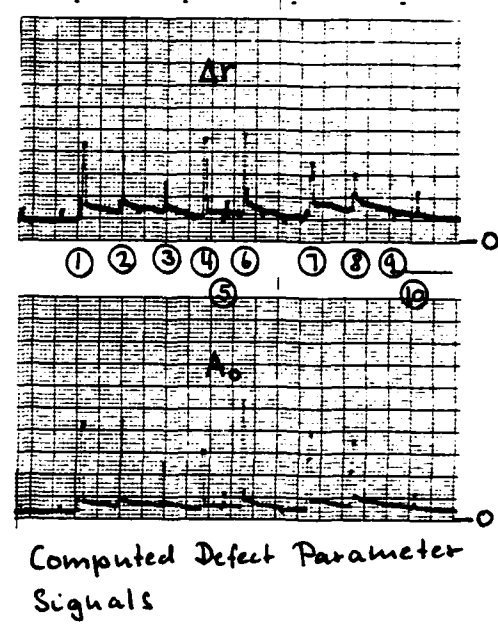
Preconditioned Signals



Modified & Peak-Sampled Signals

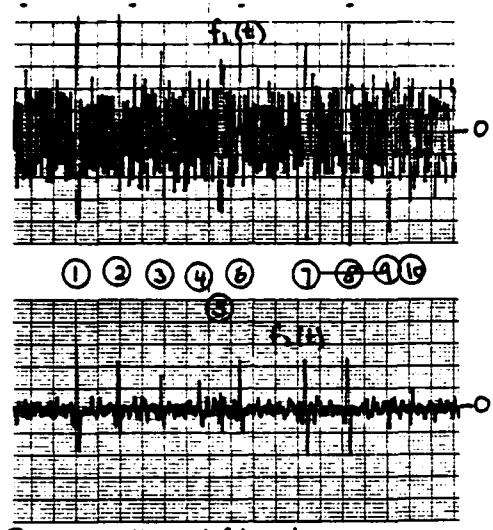


Modified Signals

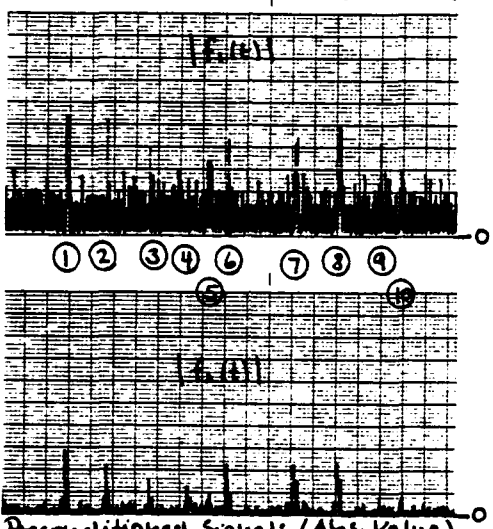


Computed Defect Parameter Signals

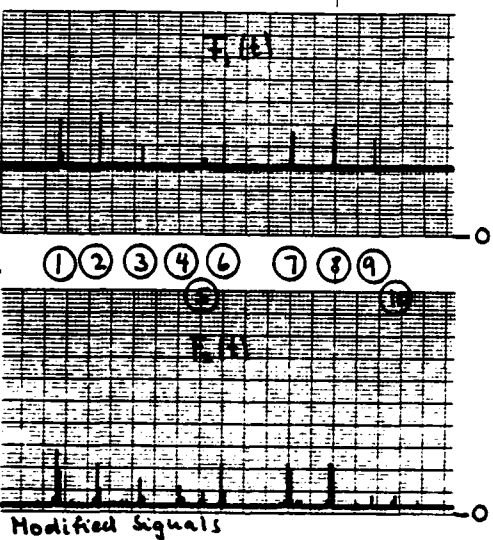
Figure 22: Test Results obtained from Test Rope



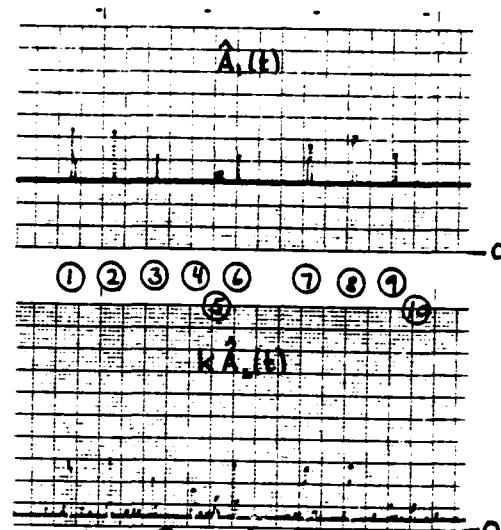
Preconditioned Signals



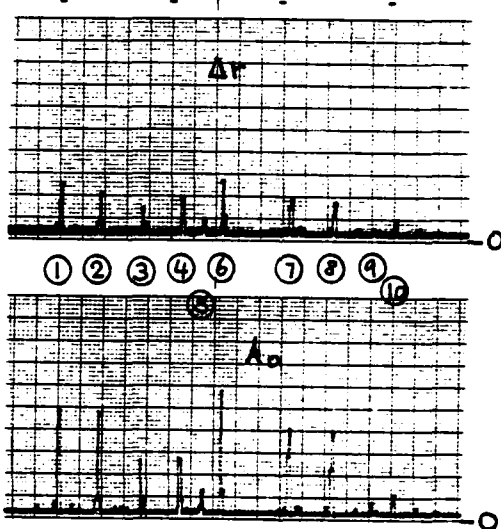
Preconditioned Signals (Abs. Value)



Modified Signals



Modified & Peak-Sampled Signals



Computed Defect Parameter Signals

Figure 23:
Test Results
obtained from Test Rope

Flaw ② and Flaw ⑥ also have identical geometries and approximately equal Fundamental Flaw Signals A_0 . Flaw ⑥ has a greater flaw distance Δr than Flaw ② which is indicated in the stripchart recordings. The wires representing Flaws ①, ⑦ and ⑧ might be too long for the mathematical model (6), (7) to be valid. Flaw ⑨ is a surface flaw with a very small (Δr) which is clearly shown. This flaw can be easily discerned in the $f_1(t)$ and $F_1(t)$ traces. However, because of its rather small physical size and because it is a surface flaw, it is hard to recognize from the signal trace A_0 . Flaw signals ⑤ and ⑩ potentially indicate internal welded wires, which occur quite frequently during the production process.

5.4 Signal-to-Noise Ratio and Repeatability

As has been discussed above, the signal-to-noise ratio and repeatability of test signals are problem areas which deserve further consideration. The hinged and subdivided sense coil arrangement has been identified as the primary culprit. Therefore, rather than trying to improve the SNR by additional signal conditioning, it is more effective to improve the test signal by an improved sensor design. It appears that sensor performance can be significantly improved by utilizing sense coils with iron cores. Among others, this proposed approach will be discussed in more detail in the forthcoming DESAT Phase II Proposal.

During the course of the present research, two attempts were made, with moderate success, to improve the SNR by signal filtering. Any filter design becomes quite complicated because all test signal frequencies are directly proportional to rope speed and are not known a priori. Therefore it is necessary to use adaptive filtering.

A cursory examination of test signals (e.g. Figures 11, 22, 23) seems to indicate that flaw pulses in general have a higher derivative (have steeper flanks) than the intrinsic noise signal. Therefore it was felt that the SNR could be improved by highpass filtering.

A simple adaptive highpass filter was designed and built. Its functional block diagram is shown in Figure 24 and Figure 25 shows the circuit implementation. The block diagram of Figure 24 is mostly self-explanatory and only a very brief description of its operation will be given.

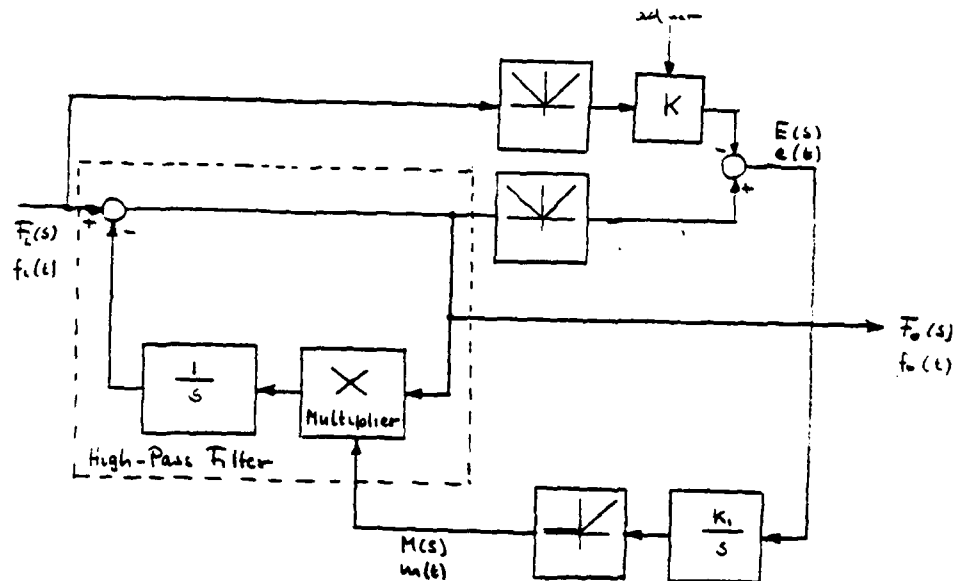


Figure 24: Adaptive Highpass Filter

The transfer function of the highpass filter is

$$G(s) = \frac{Ts}{Ts+1} \quad (13)$$

where T is adjusted adaptively by the multiplier circuit in such a fashion that, independent of signal frequency

$$\frac{f_{oav}}{f_{iav}} = k, \quad k < 1$$

where f_{iav} and f_{oav} are the mean-average-derivation (MAD) values of $f_i(t)$ and $f_o(t)$, respectively. Since, by hypothesis, the spectrum of a flaw signal contains components with higher frequencies than the underlying intrinsic noise, highpass filtering should improve the SNR. This filter could be viewed as a very simple (adaptive) matched filter.

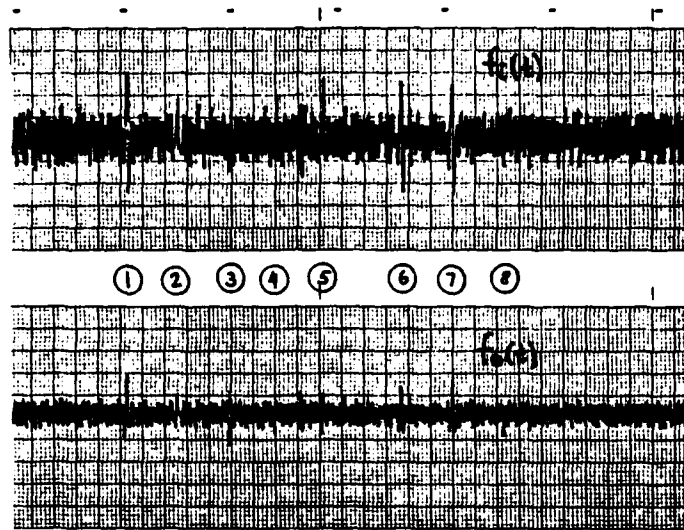


Figure 26: Results of Adaptive Highpass Filtering Experiment

Results using the filter are shown in Figure 26. For this experiment, the instrument was aligned in such a fashion that all simulated flaws were directly under the hinge of the test coils, with an associated deterioration of the SNR as discussed above. Figure 26 shows the original test signal from Coil #1 and the filtered signal with a factor $k = 0.5$.

The performance of this circuit is mixed. The SNR of Flaw ⑧, a surface flaw with a rather narrow flaw pulse was improved from approximately 1 to 1.4, which is a significant improvement. However, a slight deterioration of the SNR is observed for Flaw ②, an internal flaw with a wider pulse.

This experiment shows that an improvement of the SNR as well as reproducibility should be achieved by redesigning the coils rather than by filtering.

6. SUMMARY AND CONCLUSION

A new automatic defect characterization technique for the inspection of wire ropes has been investigated. The method consists of:

- (1) Magnetically saturating the wire rope in a longitudinal direction.
- (2) Sensing magnetic leakage fields caused by rope defects with an array of concentric test coils.
- (3) Eliminating the effects of rope speed on the test signals by a differential coil arrangement in connection with appropriate signal conditioning circuitry.
- (4) Pre-conditioning the test signals by a "Signal Modification Circuit" to eliminate non-essential portions of the test signal and to derive a measure for the fundamental noise amplitude.
- (5) Extracting essential signal parameters from the test signals by using a "Peak Sample and Hold Circuit".
- (6) Determining defect parameters from the signal parameters (transforming the signal parameter vector into the defect parameter vector) by a "Defect Parameter Computation Circuit".

The following conclusions can be drawn from this research:

- The new automatic defect characterization method is feasible.
- At the present stage, only moderate accuracy in determining defect parameters can be achieved. However, the new method is a valuable tool in estimating the flaw location and size, a very significant improvement above the present state-of-the-art in wire rope inspection.
- Major problem areas in a more accurate determination of defect parameters are the bad signal-to-noise ratio and signal repeatability. Both problems are caused by the subdivided and hinged test coil. It appears possible to remedy this situation by using test coils with iron pole pieces which will allow a more accurate guidance of the leakage flux through the test coils. This issue will be discussed further in the forthcoming DESAT Phase II Proposal.
- The use of signal filtering to improve the SNR and repeatability is only partially effective. The above mentioned improvement of the coil design is the preferred approach.
- Pulses caused by small surface flaws are suppressed by the proposed signal transformation scheme (as should be expected). This, under certain conditions, makes it hard to detect small surface flaws in the transformed signals. An improved SNR will improve this situation. Possibly an alternate form of signal display should be considered.
- Further signal parameters, such as the pulse-width of the flaw signal and/or a measure of the intrinsic signal noise spectrum, could be extracted from the test signal. The additional parameters would then allow a more detailed automatic determination of the flaw geometry.
- Relatively simple analog circuitry for signal conditioning has been used which will allow a low cost implementation of the new technique, and an operation even by moderately skilled personnel.
- With the availability of low-cost rugged and battery operated microcomputers for field use, digital signal processing will become feasible. This will allow the implementation of much more

sophisticated algorithms. This idea will be discussed in more detail in the Phase II Proposal.

- A digital computer program for the simulation of test coils has been developed. The simulation uses a magnetic dipole to model the leakage flux caused by a defect. Considering the large number of simplifying assumptions which have been made, the results of the simulation are amazingly accurate. The simulation is a valuable tool in designing improved test coils.

APPENDIX A: COMPUTER SIMULATION PROGRAM

Most attempts to analyse leakage field data are based on simple, idealized modes of defects. In spite of the numerous approximations involved in the development of such models, agreement between calculated and measured leakage field data has been surprisingly good. Some attempts are known where the leakage field of defect is represented by a dipole or by the sum of dipole fields (see (2), (8) for a further discussion). Because of its simplicity and its known relative accuracy, a dipole approximation is used here in developing a computer simulation model of the sense coil.

To develop the mathematical model, we start out with the equation for motional induction for a closed circuit (9).

$$U = \oint (\vec{v} \times \vec{B}) \cdot d\vec{l} \quad (14)$$

where

U = total emf induced in the circuit

$d\vec{l}$ = element of length of wire

\vec{v} = velocity of wire

\vec{B} = flux density of magnetic field

We compute the total induced voltage U_{ie} in a closed loop as shown in Figure 26. (Note that the terminology of the Appendix is slightly different from the terminology of the rest of this report.) Given a flux source $\Delta\phi$ in a radial distance $x < r_s$ from the z-axis of a cylindrical coordinate system and a circular path (a one turn coil) in an axial distance Δz from the flux source. Then Equation 14 becomes

$$U_{ie} = v_z \int_0^{2\pi} B_r r_s d\psi \quad (15)$$

where v_z is the (constant) velocity of the flux source relative to

(9) J.D. Kraus and K.R. Carver, "Electromagnetics" (book), Mc Graw Hill, New York, 1973, pp. 309-317

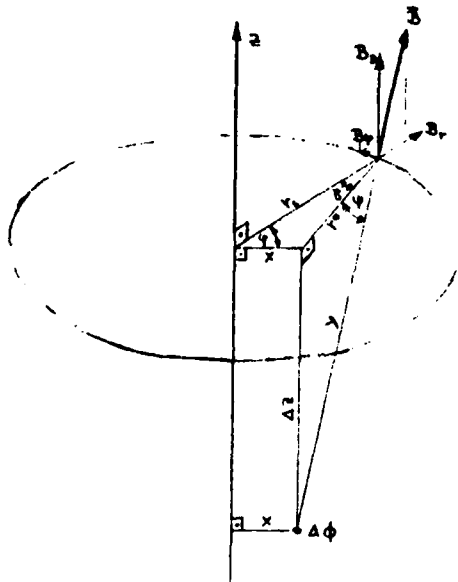


Figure 27: Computation of Motional Induction

the coil and U_{ie} is the total voltage induced in the coil. Then we have the following geometric relations

$$y^2 = \Delta z^2 + r^{*2}$$

$$r^{*2} = r_s^2 + x^2 - 2r_s x \cos \psi \quad (16)$$

$$x^2 = r^{*2} + r_s^2 - 2r^* r_s \cos \gamma \quad (17)$$

$$B_r = |B| \cos \psi \cos \gamma = \frac{\Delta \phi}{4\pi y^2} \frac{r^*}{y} \cos \gamma \quad (18)$$

or

$$B_r = \frac{\Delta \phi}{4\pi} \frac{r_s - x \cos \psi}{(r_s^2 + x^2 - 2r_s x \cos \psi + \Delta z^2)^{3/2}} \quad (19)$$

To compute the integral (15) in the computer simulation, the circular path is subdivided into 100 sections and then the computed points are summed up. Because of symmetry it is sufficient to compute 50 points

$$\int_0^{2\pi} B_r d\varphi = \frac{\Delta \phi}{200\pi} \sum_{n=1}^{50} \frac{r_n^{*2} + r_s^2 - x^2}{(r_n^{*2} + z^2)^{3/2}} \quad (20)$$

where

$$r_n^{*2} = r_s^2 + x^2 - 2r_s x \cos \varphi_n$$

$$\varphi_n = \frac{\pi}{50} (n - \frac{1}{2})$$

The computation is performed by the program SGLPO/SGL which was written in BASIC for a TRS80 Color Computer. The program is listed in Table 2. SGLPO/SGL computes the induced voltage in a single circular coil, caused by the radial leakage field of an excentrically located single pole for a range of values of z .

The computation of the combined voltages in a set of coils according to Figure 6 is performed by the Program DIPO/MLT which is listed in Table 3. This program uses the data generated by SGLPO/SGL to compute (by linear superposition) the induced voltage in a set of coils, caused by the radial leakage field of a dipole. Integration of coil voltages along the z -axis (or along the t -axis, since v_z is constant) is performed approximately by summation of the induced voltages for each value of Δz . Figure 28 shows results obtained from the computer simulation. Parameters of the simulation correspond to the parameters of the experiments described in Chapter 4 which are shown in Figure 10. Note, however, that the

```

10 "SGLPO/SGL" OF 21 JUNE 1982 ON DISK
20 'THE PROGRAM COMPUTES THE INDUCED VOLTAGE IN A SINGLE COIL, CAUSED BY THE RAD
IAL LEAKAGE FIELD OF A SINGLE POLE
30 '
40 PRINT#-2,TAB(20);"PROGRAM SGLPO/SGL OF 21 JUNE 1982"
50 CLS0:PRINT "TYPE A COMMENT:"
60 LINE INPUT A$
70 PRINT#-2,A$;PRINT#-2,"
80 'MODIFIED PROGRAM "RADIALE"
90 DIM UI(120),V1(50),XX(10),ADX(10),RSX(10)
100 'INPUT OF INITIAL VALUES
110 OPEN"0",#1,"MONO/DAT"
120 INPUT "NUMBER OF CONDITIONS=";NI
130 WRITE #1,NI
140 FOR NJ=1 TO NI
150 INPUT "FLAW RADIUS X=";XX(NJ)
160 INPUT "COIL RADIUS RS=";RSX(NJ)
170 NEXT NJ
180 FOR NJ=1 TO NI
190 X=XX(NJ)
200 RS=RSX(NJ)
210 WRITE #1,X,RS
220 W1=+1;W2=-1;W3=-1;W4=+1
230 D=.0010;VZ=1;FD=1E-06
240 KM=60
250 'PRINT INITIAL VALUES
260 CLS0:PRINT#-2,TAB(20);"PARAMETERS"
270 PRINT#-2,"D=";D,"RS=";RS;PRINT#-2,"X=";X,"VZ=";VZ,"FID=";FD,"KM=";KM
280 'COMPUTE SEVERAL CONSTANTS
290 U1=RS^2-X^2
300 U2=.005*VZ*FD
310 U3=RS^2+X^2
320 U4=2*RS*X
330 GOSUB 500
340 PRINT#-2,TAB(12);"INDUCED VOLTAGE"
350 'COMPUTATION OF INDUCED VOLTAGE IN A SINGLE COIL
360 GOSUB 410
370 NEXT NJ
380 CLOSE #1
390 GO TO 390
400 END
410 'SUBROUTINE EXUI
420 'INPUT IS AD,KM,RS,U1,U2,U3,U4,D,ZM,V1(50),KI,FI,KZ,D1,D2
430 'OUTPUT IS UI(500)
440 FOR KI=1 TO 50
450 V1(KI)=U3-(U4*COS(.062831853*(KI-.5))):NEXT KI
460 FOR KZ=1 TO KM
470 D1=KZ*D-60*D
480 UI(KZ)=0.
490 FOR KI=1 TO 50
500 UI(KZ)=UI(KZ)+((U2*(U1+V1(KI)))*(1./SQRT((V1(KI)+D1^2)^3)))
510 NEXT KI
520 PRINT#-2,"KZ=";KZ," DEZ1=";D1;" DEZ2=";D2;" UI=";UI(KZ)
530 ZZ=95-INT(UI(KZ)*1.E06 + .5)
540 WRITE #1,KZ,UI(KZ)
550 PSET(5+2*KZ,ZZ,1)
560 NEXT KZ
570 RETURN
580 ' CLEAR THE SCREEN
590 PMODE 4,1:PCLS:SCREEN 1,0
600 LINE (5,5)-(5,185),PSET:LINE(5,95)-(245,95),PSET:LINE(245,5)-(245,185),PSET
610 FOR XS=5 TO 247 STEP 6:PRESET(XS,95):NEXT
620 FOR YS=5 TO 185 STEP 15:PRESET(5,YS):PRESET(245,YS):NEXT
630 RETURN
640 CLS0
650 GOTO650

```

Table 2

```

10 CLEAR 200,&H7DFF
20 LOADM"GSPPR/BIN"
30 DEFUSR1=&H7E00
40 "DIPO/MLT" OF 21 JUNE 1982 ON DISK
50 'THE PROGRAM COMPUTES THE INDUCED VOLTAGE IN A SET OF COILS, CAUSED BY THE RA
DIAL LEAKAGE FIELD OF A DIPOLE
60 '
70 PRINT#-2,TAB(20);"PROGRAM DIPO/MLT OF 21 JUNE 1982"
80 CLS0:PRINT "TYPE A COMMENT:"
90 LINE INPUT A$
100 PRINT#-2,A$;PRINT#-2,""
110 DIM UX(120,10),V1(50),XX(10),AX(10),RX(10),DX(100),DY(100),UI(120)
120 OPEN "I",#1,"MONO/DAT"
130 D=.0005;VZ=1;FD=1E-06
140 W1=1;W2=-1;W3=-1;W4=1
150 INPUT#1,NI
160 FOR NJ=1 TO NI
170 INPUT#1,XX(NJ),RX(NJ)
180 KM=60
190 FOR KY=1 TO KM
200 INPUT#1,KZ,UX(KZ,NJ)
210 UX(120-KZ,NJ)=UX(KZ,NJ)
220 NEXT KY
230 NEXT NJ
240 CLOSE#1
250 INPUT "SPACINGS S,BP:";S,BP
260 INPUT "DIPOLE SPACING=";AD
270 FOR NJ=1 TO NI
280 X=XX(NJ)
290 RS=RX(NJ)
300 'PRINT INITIAL VALUES
310 CLS0:PRINT#-2,TAB(20);"INITIAL VALUES"
320 PRINT#-2,"AD=";AD,"D=";D,"RS=";RS;PRINT#-2,"X=";X,"VZ=";VZ,"FID=";FD,"BSP=";
BP,"S=";S
330 'COMPUTE SEVERAL CONSTANTS
340 U1=RS^2-X^2
350 U2=.005*VZ*FD
360 U3=RS^2+X^2
370 U4=2*RS*X
380 GOSUB 850
390 PRINT#-2,TAB(12);"PARTIAL INDUCED VOLTAGE"
400 GOSUB 690
410 GOSUB850
420 'COMPUTATION OF INDUCED VOLTAGE IN THE COIL
430 'ASSUME FOUR COILS OF OUTER SEPARATIONS =S , AND INNER SEPARATION =BP
440 'VOLTAGE WEIGHTS W1,W2,W3,W4
450 IP=INT(SP/(2*D)+.5)
460 I2=INT(S/D+.5)
470 KH=INT(ZM/(2*D)+.5)+1
480 KU=IP+1+I2+KH
490 PRINT#-2,"";PRINT#-2," RESULT OF RADIAL COILS FOR THE FOLLOWING
CONDITIONS:"
500 PRINT#-2,"COIL WEIGHTS ARE 'W1;W2;W3;W4"
510 PRINT#-2,"D=";D;" METERS";PRINT#-2,"AD=";AD;" METERS"
520 PRINT#-2,"X=";X;" METERS";PRINT#-2,"FID=";FD;" VS"
530 PRINT#-2,"VZ=";VZ;" M/S";PRINT#-2,"RS=";RS;" METERS"
540 PRINT#-2,"BSP=";BP;" METERS","S=";S;PRINT#-2,TAB(10);"U2
IZ"
550 IZ=0; IZ IS THE SPATIAL INTEGRAL OF U4
560 FOR KZ=KU TO 60
570 'PRINT RESULTS
580 U4=W1*UI(KZ+IP+I2)+W2*UI(KZ+IP)+W3*UI(KZ-IP)+W4*UI(KZ-IP-I2)
590 IZ=IZ-U4
600 U2=UI(KZ+IP+I2)-UI(KZ-IP-I2)
610 PRINT#-2,KZ;U2;U4;IZ
620 ZZ=95-INT(U2*1.E06+.5);XS=5+2*KZ;XT=245-2*KZ;PSET(XS,ZZ,1);PSET(XT,ZZ,1)
630 ZZ=95-INT(IZ*0.2E06+.5);PSET(XS,ZZ,1);PSET(XT,ZZ,1)
640 NEXT KZ
650 P=USR1(0)
660 GOSUB 850
670 NEXT NJ
680 GO TO 250
690 'SUBROUTINE EXUI
700 'INPUT IS AD,KM,RS,U1,U2,U3,U4,D,ZM,V1(50),K1,F1,KZ,D1,D2
710 'OUTPUT IS UI(100)
720 KD=INT(AD/(2*D)+.5)
730 FOR KZ=(KD+1) TO 60
740 D1=KZ*D
750 UI(KZ)=UX(KZ-KD,NJ)-UX(KZ+KD,NJ)
760 UI(120-KZ)=-UI(KZ)
770 PRINT#-2,"KZ=";KZ," DEZ1=";D1;" DEZ2=";D2;" UI=";UI(KZ)
780 ZZ=95-INT(UI(KZ)*1.E06+.5)
790 ZT=95+INT(UI(KZ)*1.E06+.5)
800 PSET(5+2*KZ,ZZ,1)
810 PSET(245-2*KZ,ZT,1)
820 NEXT KZ
830 P=USR1(0)
840 RETURN
850 ' CLEAR THE SCREEN
860 PHODE 4,1;PCLS;SCREEN 1,0
870 LINE(5,5)-(5,185),PSET;LINE(5,95)-(245,95),PSET;LINE(245,5)-(245,185),PSET;
LINE(125,5)-(125,185),PSET;LINE(5,5)-(245,5),PSET;LINE(5,185)-(245,185),PSET
880 FOR XS=5 TO 245 STEP 5:PSET(XS,95);PSET(XS,5);PSET(XS,185);NEXT
890 FOR YS=5 TO 185 STEP 10:PSET(5,YS);PSET(245,YS);PSET(125,YS);NEXT
900 RETURN

```

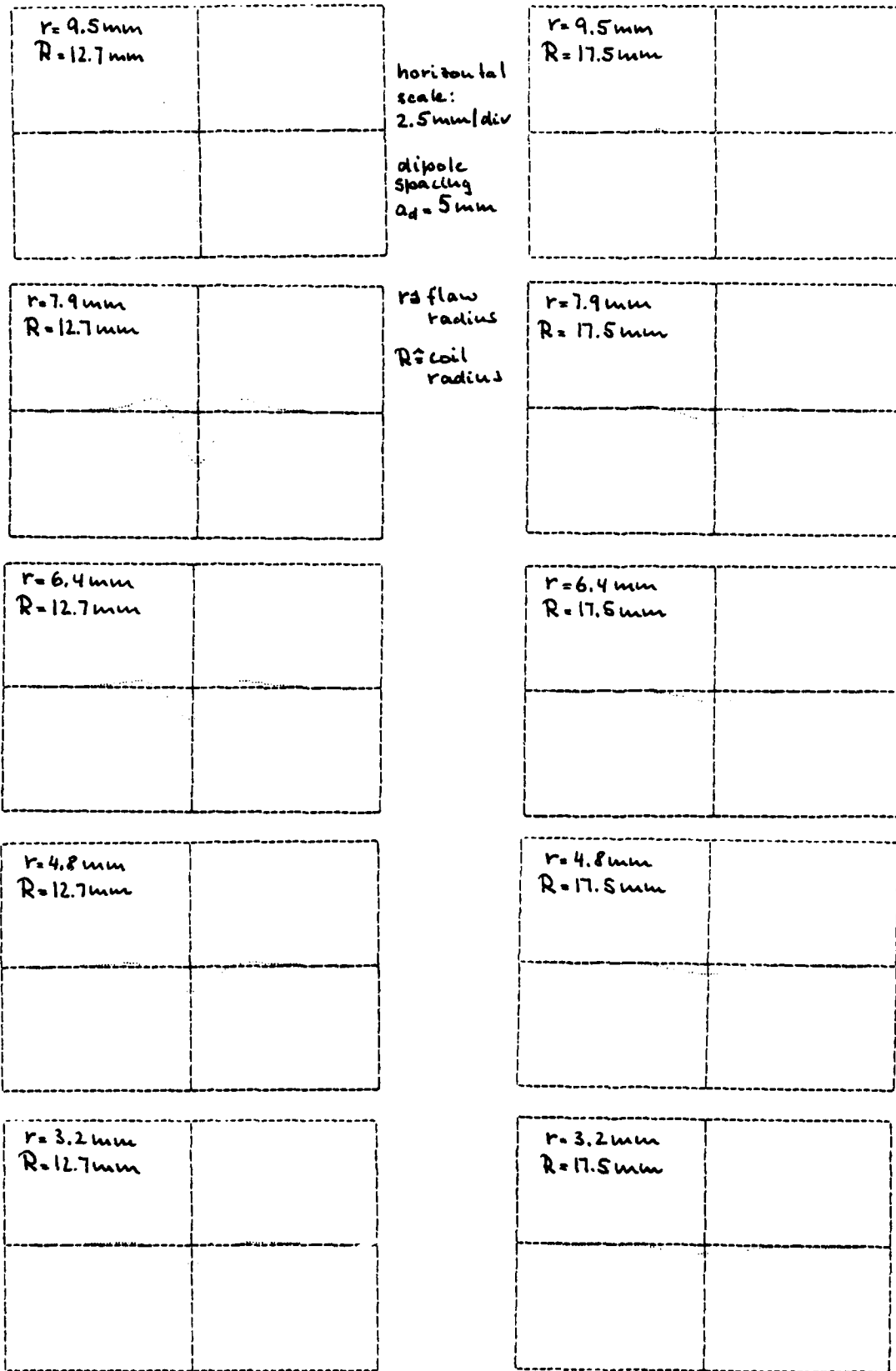


Figure 28: Results of Coil Simulation

1.2 mm diameter holes in the experiments are simulated by a dipole with spacing $a_d = 5$ mm. It is a known fact (see (2)) that, for all dipole models, the dipole spacing has to be chosen significantly larger than the dimensions of the simulated flaw. This is true especially for very small flaws. With the above reservation, experimental and simulation results are in very good agreement. The computer simulation is an excellent tool for designing sense coils.

ME
8